Chapter 3

Wide-Field and Two-Photon Imaging of Brain Activity with Voltage- and Calcium-Sensitive Dyes

Ryota Homma, Bradley J. Baker, Lei Jin, Olga Garaschuk, Arthur Konnerth, Lawrence B. Cohen, Chun X. Bleau, Marco Canepari, Maja Djurisic and Dejan Zecevic

Abstract

This chapter presents three examples of imaging brain activity with voltage- or calcium-sensitive dyes. Because experimental measurements are limited by low sensitivity, the chapter then discusses the methodological aspects that are critical for optimal signal-to-noise ratio. Two of the examples use wide-field (1-photon) imaging and the third uses two-photon scanning microscopy. These methods have relatively high temporal resolution ranging from 10 to 10,000 Hz.

The three examples are the following: (1) Internally injected voltage-sensitive dye can be used to monitor membrane potential in the dendrites of invertebrate and vertebrate neurons in in vitro preparations. These experiments are directed at understanding how individual neurons convert the complex input synaptic activity into the output spike train. (2) Recently developed methods for staining many individual cells in the mammalian brain with calcium-sensitive dyes together with two-photon microscopy made it possible to follow the spike activity of many neurons simultaneously while in vivo preparations are responding to stimulation. (3) Calcium-sensitive dyes that are internalized into olfactory receptor neurons in the nose will, after several days, be transported to the nerve terminals of these cells in the olfactory bulb glomeruli. There, the population signals can be used as a measure of the input from the nose to the bulb.

Three kinds of noise in measuring light intensity are discussed: (1) Shot noise from the random emission of photons from the preparation. (2) Extraneous (technical) noise from external sources. (3) Noise that occurs in the absence of light, the dark noise. In addition, we briefly discuss the light sources, the optics, and the detectors and cameras.

The commonly used organic voltage and ion sensitive dyes stain all of the cell types in the preparation indiscriminately. A major effort is underway to find methods for staining individual cell types in the brain selectively. Most of these efforts center around fluorescent protein activity sensors because transgenic methods can be used to express them in individual cell types.

Fahmeed Hyder (ed.), *Dynamic Brain Imaging: Multi-Modal Methods and In Vivo Applications, vol. 489*

DOI 10.1007/978-1-59745-543-5_3 Springerprotocols.com

Key words: Two-photon microscopy, one-photon (wide-field) microscopy, voltage-sensitive dyes, calcium-sensitive dyes, neural networks.

1. Introduction

An optical measurement of brain activity using a molecular probe can be beneficial in a variety of circumstances. An obvious advantage of any imaging method is the possibility of simultaneous measurements from many locations. This is especially important in the study of the nervous system where many parts of an individual cell, or many cells, or many regions, are simultaneously active. In addition, optical recording offers the possibility of recording from processes which are too small or fragile for electrode recording.

An important advantage of optical methods for measuring activity is their relatively high spatial resolution. In one of the examples presented below, the resolution is on the order of a few microns; in another, it is easy to distinguish the activity of individual cells. However, optical recordings are generally limited to areas of the brain that can be visualized and, in these areas, limited to a recording depth of about 0.5 mm.

Using a molecular probe has advantages (and disadvantages) over intrinsic signals. For optical imaging of membrane potential, the use of molecular probes has resulted in greatly increased signal size in comparison to intrinsic signals. Furthermore, with the introduction of protein activity sensors, there is now the possibility for cell type specificity. In addition, many of the molecular probes are fast with a time resolution in microseconds or milliseconds but others, especially the protein-based biosensors, are substantially slower. Finally, there are novel probes that are sensitive to various ions and metabolic intermediates. With these advantages comes the responsibility for demonstrating that pharmacological and photodynamic effects are minimal (see below).

1.1. Voltage-Sensitive Dyes

Several different optical properties of membrane-bound organic dyes are sensitive to membrane potential including fluorescence, absorption, dichroism, birefringence, Förster resonance energy transfer (FRET), non-linear second harmonic generation, and resonance Raman absorption. Similarly, another group of organic dyes are sensitive to ion concentrations. However, because the vast majority of applications have involved fluorescence or absorption measurements, these will be the only subjects of this review.

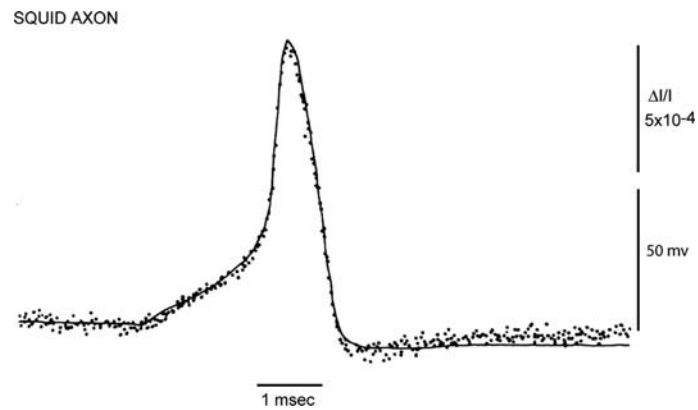

Fig. 3.1. Changes in absorption (dots) of a giant axon stained with a merocyanine dye, XVII (**F**ig. 3.2), during a membrane action potential (smooth trace) recorded simultaneously. The change in absorption and the action potential had the same time course. In this and subsequent figures, the size of the vertical line represents the stated value of the fractional change in intensity of transmitted (ΔI/I), or fluorescent (ΔF/F) light. The response time constant of the light measuring system was 35 μsec; 32 sweeps were averaged. Modified from Ross et al. *(59)*.

The voltage-sensitive dye signals described in this chapter are "fast" signals *(1)* that are presumed to arise from membrane-bound dye; they follow changes in membrane potential with a time course that is rapid compared to the rise time of an action potential. **Figure 3.1** illustrates the kind of result that is used to define a voltage-sensitive dye. In a model preparation, the giant axon from a squid, these optical signals are fast, following membrane potential with a time constant of $<$10 μsec *(2)* and their size is linearly related to the size of the change in potential (e.g. *(3)*). Thus, these dyes provide a direct, fast, and linear measure of the change in membrane potential of the stained membranes.

Several voltage-sensitive dyes (e.g., **Fig. 3.2A**) have been used to monitor changes in membrane potential in a variety of preparations. This figure illustrates four different chromophores (the merocyanine dye, XVII, was used for the measurement illustrated in **Fig. 3.1**). For each chromophore, approximately 100 analogues have been synthesized in an attempt to optimize the signal-to-noise ratio that can be obtained in a variety of preparations. (This screening was made possible by synthetic efforts of three laboratories: Jeff Wang, Ravender Gupta and Alan Waggoner then at Amherst College; Rina Hildesheim and Amiram Grinvald at the Weizmann Institute; and Joe Wuskell and Leslie Loew at the University of Connecticut Health Center.) For each of the four chromophores illustrated in **Fig. 3.2**, there were 10 or 20 dyes that gave approximately the same signal size on squid axons *(3)*. However, dyes that had nearly identical signal size on squid axons could have very different responses in other

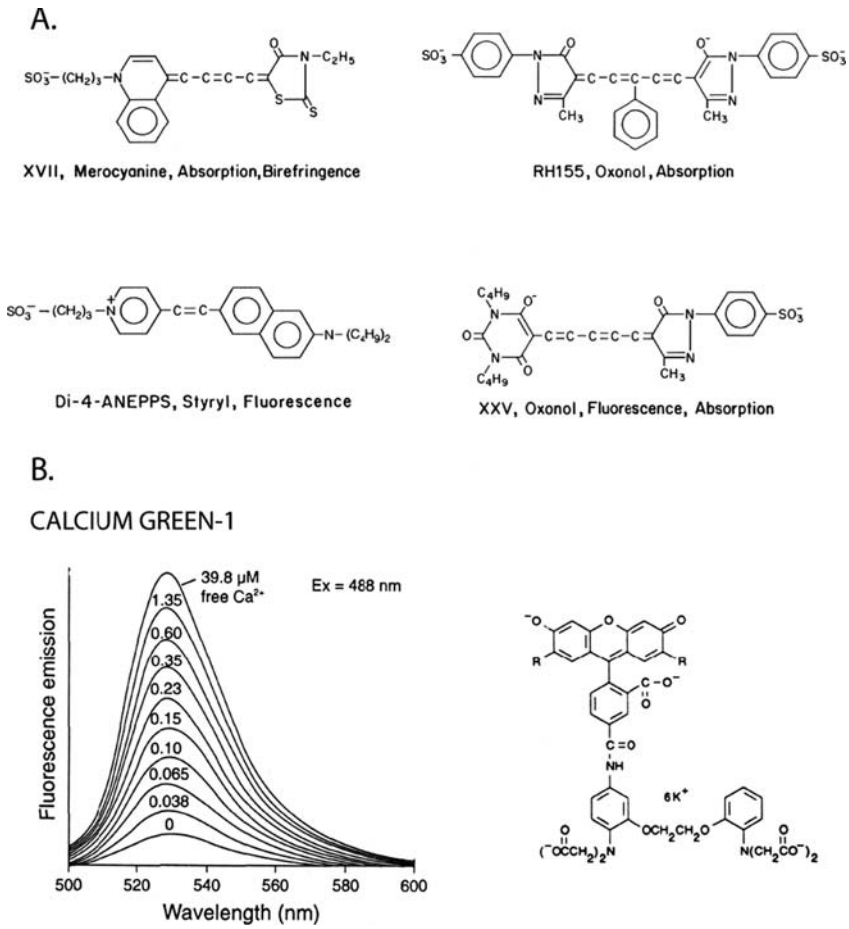

Fig. 3.2. A. Examples of four different chromophores that have been used to monitor membrane potential. The oxonol dye, RH155, and its analog RH482 (not shown), are commercially available as NK3041 and NK3630 from Hayashibara Biochemical Laboratories Inc./Kankoh-Shikiso Kenkyusho Co. Ltd., Okayama, Japan. The oxonol, XXV (WW781) and styryl, di-4-ANEPPS, are available commercially as dye R-1114 and D-1199 from Invitrogen Molecular Probes, Junction City, OR. Merocyanine dyes, including XVII (WW375, NK2495), and its analog, NK2761, need negotiation with Hayashibara Biochemical Laboratories. **B**. The chemical structure (*right*) and the emission spectrum as a function of calcium concentration of Calcium Green-1. The conjugate with the 10 kD dextran is available commercially from Molecular Probes as C-3713. Data taken from the Handbook of Fluorescent Probes and Research Chemicals, sixth edition, Molecular Probes.

preparations, and thus, tens of dyes usually have to be tested to obtain the largest possible signal. A common problem was that the dye did not penetrate through connective tissue or along intercellular spaces to the membrane of interest.

The following rules-of-thumb seem to be useful: First, each of the chromophores is available with a fixed charge which is either a quaternary nitrogen (positive) or a sulfonate (negative). Generally, the positively charged dyes have given larger signals in vertebrate preparations. Second, each chromophore is available with carbon chains of various lengths. The more hydrophilic dyes (methyl or ethyl) work best if the dye has to penetrate through

a compact tissue (vertebrate brain) or needs to travel a long distance in a dendritic tree.

A number of studies have been conducted to determine the molecular mechanisms that result in potential-dependent optical properties. The available evidence supports three different mechanisms (for different dyes): Dipole rotation *(5)*, electrochromism *(2)*, and a potential sensitive monomer-dimer equilibrium *(4)*. In many cases, it has been possible to show that pharmacological and photodynamic effects are small (e.g. *(6–12)*).

1.2. Calcium-Sensitive Dyes

Figure 3.2B shows the chemical structure of a calcium-sensitive dye, Calcium Green-1, together with a plot of the fluorescence spectrum as a function of the free calcium concentration. This dye signal reaches 50% of its maximum at a calcium concentration of about 0.2 μM. In contrast to the voltage-sensitive dyes, the calcium dyes are located intracellularly. The dye is presumed to be in the cytoplasm and to report changes in the calcium concentration in the cytoplasm, although some of the dye may be in other intracellular compartments. These dyes are slower to respond and, because they also act as buffers of calcium, the calcium signal in the presence of dye may substantially outlast the change in calcium concentration that would occur in the absence of the dye *(13, 14)*.

We begin with examples obtained from measurements addressing three quite different neurobiological problems. In one example where the light level was low, the camera was a fast, back-illuminated, CCD camera with 80×80 pixel spatial resolution. In the second example, cellular resolution could only be obtained using two-photon scanning microscopy. In the third example, a slower CCD camera with 256×256 pixel spatial resolution was used. The optical signals in the three examples are not large, they represent fractional changes in light intensity ($\Delta I/I$) of from $5\times10^{-3}$to 5×10^{-1} and have modest signal-to-noise ratios. Nonetheless, they can be measured with an acceptable signal-to-noise ratio after attention to details of the measurement which are described in the second part of the chapter.

Figure 3.3 illustrates the three qualitatively different applications in neurobiology where imaging has been useful. First (left panel), in order to know how a neuron integrates its synaptic input into its action potential output, one needs to be able to measure membrane potential everywhere where synaptic input occurs and at the places where spikes are initiated. Second (middle panel), in order to understand how a nervous system generates a behavior, it is important to measure the action potential activity of many of the participating neurons. Third (right panel), responses to sensory stimuli and generation of motor output in the vertebrate brain are often accompanied by synchronous

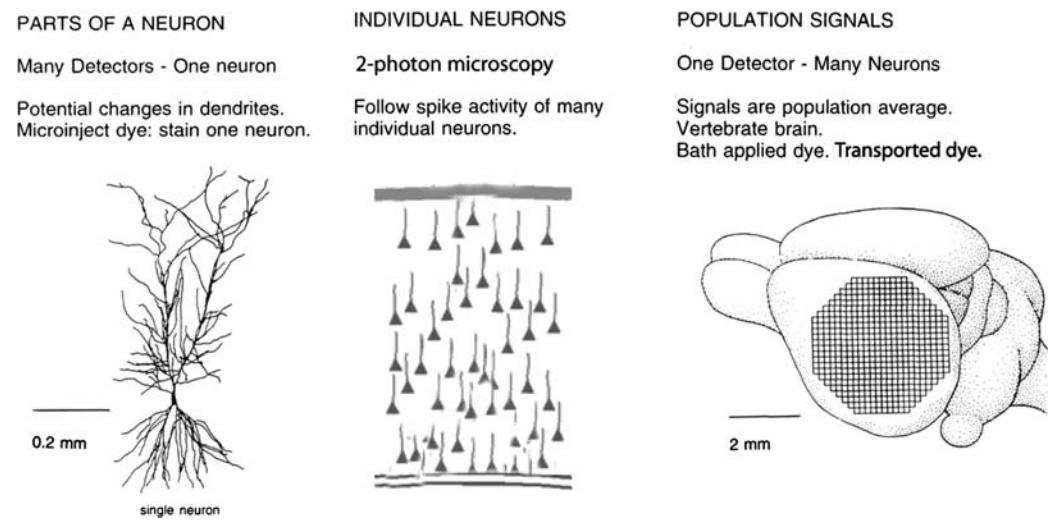

Fig. 3.3. Schematic drawings of the three kinds of measurements described as examples. *Left*, an individual cortical hippocampal CA1 pyramidal cell. Each pixel of an 80×80 pixel CCD camera would receive light from a small part of the dendrite, axon, or cell body of the neuron. An optical measurement of membrane potential would provide important information about how the neuron converts its synaptic input into its spike output. *Middle*, a drawing of cells in a vertebrate cortex. 2-photon imaging allows imaging of the fluorescence of many individual neurons stained with a calcium sensitive dye. *Right*, a vertebrate brain with a superimposed pixel array. Each pixel of the array would receive light from thousands of cells and processes. The signal would be the population average of the change in membrane potential in those cells and processes.

activation of many neurons in wide-spread brain areas; optical imaging allow simultaneous measurement of population signals from many areas. In these three instances, optical recordings have provided kinds of information about the function of the nervous system that were previously unobtainable.

2. Three Examples

2.1. Processes of an Individual Neuron (Fig. 3.3, Left Panel)

Understanding the biophysical properties of single neurons and how they process information is fundamental to understanding how the brain works. At present, however, the detailed functional structure of nerve cells is not fully understood. Part of the explanation for this incomplete understanding is that neurons are exceedingly complex. It is widely recognized that dendritic membranes of many vertebrate CNS neurons contain active conductances such as voltage-activated Na^+, Ca^{2+} and K^+ channels (e.g. *(15–20)*). An important consequence of active dendrites is that regional electrical properties of branching neuronal processes will be extraordinarily complex, dynamic, and, in the general case, impossible to predict in the absence of detailed measurements. To obtain such a measurement, one would, ideally, like to be able

to monitor, at multiple sites, subthreshold events as they travel from the sites of origin on neuronal processes and summate at particular locations to influence action potential initiation. This can be achieved by using voltage-imaging. Recently, the sensitivity of intracellular voltage-sensitive dye technique has been dramatically improved allowing direct recording of subthreshold and action potential signals from the neurites of individual neurons *(10–12, 21–24)*.

2.1.1. Dye Screening

We carried out experiments to develop a methodology for optical monitoring of the generation and spread of subthreshold synaptic potentials and action potentials in neuronal processes using selective staining of individual invertebrate and vertebrate neurons by intracellular application of membrane impermeant voltage-sensitive dyes *(25)*. First, we tested analogues of the most successful absorption dyes known from extracellular application because absorption dyes were substantially better in terms of photodynamic damage as compared to fluorescence dyes. A total of 30 dyes were tested. The best results were obtained with two positively-charged pyrazolone-oxonol dyes (designated JPW1177 and JPW1245), and two negatively-charged merocyanine dyes (designated WW375 and JPW1124). However, the signal-to-noise ratio for the best dyes in these series varied from 1 to 4 in single trials. We concluded that this mode was probably not sensitive enough to allow monitoring neuronal signals from distal processes.

Fluorescence measurements are more effective than absorption measurements in the situation where the image of the object (e.g. thin process) is much smaller than the size of a photodetector *(6, 26)*. We found that JPW1114 was better than the three other fluorescent styryl molecules we tested (RH461, RH437 and JPW1063) as determined by signal-to-noise ratio. There was an improvement in sensitivity (as defined by the signal-to-noise ratio) by a factor of about 50 over previously reported (e.g. *(27, 28)*) absorption and fluorescence signals from neuronal processes stained by either intra- or extracellular application of dyes *(25)*. The obtained sensitivity depends on using fluorescence measurements and selective staining of only one neuron within a ganglion *(29)*, and, on finding a dye that gives relatively large signals when applied internally. The fluorescent voltage-sensitive styryl dye JPW1114 (also called di-2-ANEPEQ), is a doubly positively charged analog of the ANEPPS series of lipophilic voltage sensitive dyes that is still sufficiently water soluble to be used for microinjection. JPW1114 (available from Invitrogen - Molecular Probes Inc. as D6923), together with its close analog JPW3028 (di-1-ANEPEQ), is presently the optimal voltage indicator for intracellular application in recording from neuronal processes of individual neurons in brain slices *(12, 23)*.

2.1.2. Methods

We use a stationary stage upright microscope equipped with two camera ports. One port has a standard high spatial resolution CCD camera for infrared differential interference contrast video-microscopy. The other camera port has a fast data acquisition camera with relatively low spatial resolution (80×80 pixels) but outstanding dynamic range (14 bits; NeuroCCD-SM, RedShirtImaging LLC, Decatur, GA). The analysis and display of data are carried out using the NeuroPlex program (RedShirtImaging) written in IDL (ITT Visual Information Solutions, Boulder, Colorado) running on a Windows XP computer. The brain slice is placed on the stage of the microscope and the fluorescent image of the stained cell projected by a water immersion objective via an optical coupler (0.09–0.11 X; RedShirtImaging) onto the CCD chip. A 250 W xenon, short-gap, arc lamp (Osram, XBO 250 W/CR ORF) powered by a low ripple power supply (Model 1700XT/A, Opti-Quip, Highland Mills, NY) is the source of excitation light.

With the above dye, the best signals are obtained using an excitation interference filter of 520±45 nm, a dichroic mirror with the central wavelength of 570 nm, and a 610 nm barrier filter (a Schott RG610). With the sensitivity of the intracellular voltage-sensitive dyes used (1–6% $\Delta F/F$ per 100 mV in recording from dendritic processes), relatively good signal-to-noise ratios can be obtained in single-trial recordings with modest spatial averaging (4–10 pixels) from dendritic regions that are about 300 μm away from the soma. Modest signal-averaging (4 trials) is often used to improve the signal-to-noise ratio further.

In experiments where calcium and voltage imaging is carried out from the same neuron, Ca^{2+} signals are recorded at the frame rate of 500 Hz using an excitation interference filter of 380±15 nm, a dichroic mirror with central wavelength of 400 nm and a 450 nm barrier filter. Calcium fluorescence transients are expressed as $\Delta F/F=(F_0-F)/F_0$, where F is the stimulated fluorescence and F_0 is the resting fluorescence. The value of F is calculated after subtracting auto-fluorescence determined for an area far from the loaded dendrite. Due to uneven illumination of the field of view and due to differences in auto-fluorescence between different parts of the slice, background fluorescence values vary between different regions on the same slice typically by a factor of up to 3. However, when signals from the same dendritic regions are compared under different conditions, possible errors in calculating $\Delta F/F$ introduced by uncertainties about actual contribution of auto-fluorescence to the resting light intensity can be neglected. We did not detect any toxicity of $[Ca^{2+}]_i$ indicator bis-fura-2; loading of neurons did not have detectable pharmacological effects (toxicity of the indicator dye in the absence of excitation light) on the electrical behavior of neurons. During

calcium imaging, the exposure of the preparation to the excitation light was limited to the recording periods of 400 ms.

Even after 50–100 recording trials, typically collected for one experiment, no change has been found in the amplitude or the time course of optical or electrical signals due to photodynamic damage (toxicity induced by the interaction of the indicator dye with high intensity light).

The voltage-sensitive dyes, JPW 1114 or JPW 3028, have little or no pharmacological effect when applied at functional concentrations to both invertebrate *(22, 25)* and vertebrate neurons *(11, 12, 21, 23, 24)*. We also demonstrated, for invertebrate neurons, rat neocortical layer V and hippocampal CA1 pyramidal neurons, and mitral cells of the olfactory bulb, that photodynamic damage during optical recording was not present if the exposures of the dendritic arbor to excitation light were kept relatively short (100 ms) and if successive trials were separated by dark intervals lasting several minutes *(10, 12, 21, 23, 24)*.

2.1.3. Example Results

The current sensitivity of voltage imaging allowed experiments in which subthreshold, synaptic potentials were monitored at the site of origin, in the dendritic tuft of mitral cells in the olfactory bulb of the rat. **Figure 3.4-I** illustrates presently available signal-to-noise ratio obtained at the desired spatial resolution. Our results showed consistently that the highest sensitivity was achieved in recording from thin terminal branches in the mitral cell tuft, likely due to the favorable surface-to-volume ratio of these structures. The effect is based on the fact that, in addition to the plasma membrane, the cytoplasm and the internal membranes (e.g. ER membranes, mitochondria) of the stained cell also contain the dye. Dye bound to internal membranes does not contribute to the signal because it is not in the membrane that changes potential. This internal dye, nonetheless, contributes to the resting fluorescence and degrades the fractional change in light intensity ($\Delta F/F$). In addition, the higher sensitivity of recording from the tuft is accompanied by an improved signal-to-noise ratio (for the same $\Delta F/F$) based on a large membrane surface area of the terminal dendritic arborization. Larger membrane surface area results in the larger amount of the membrane bound dye and higher light intensity; higher light intensity, in turn, results in the higher signal-to-noise ratio under our experimental conditions (dominant noise is statistical, shot noise). This is a fortunate feature of voltage imaging because thin dendritic branches receive all of the excitatory synaptic inputs in mitral cells, are not accessible to direct electrical measurement, and are likely to be a key compartment for signal integration.

Figure 3.4-I illustrates the spatial resolution and the sensitivity of voltage imaging from small dendritic structures (single pixels received light from 4×4 μm areas in the object plane).

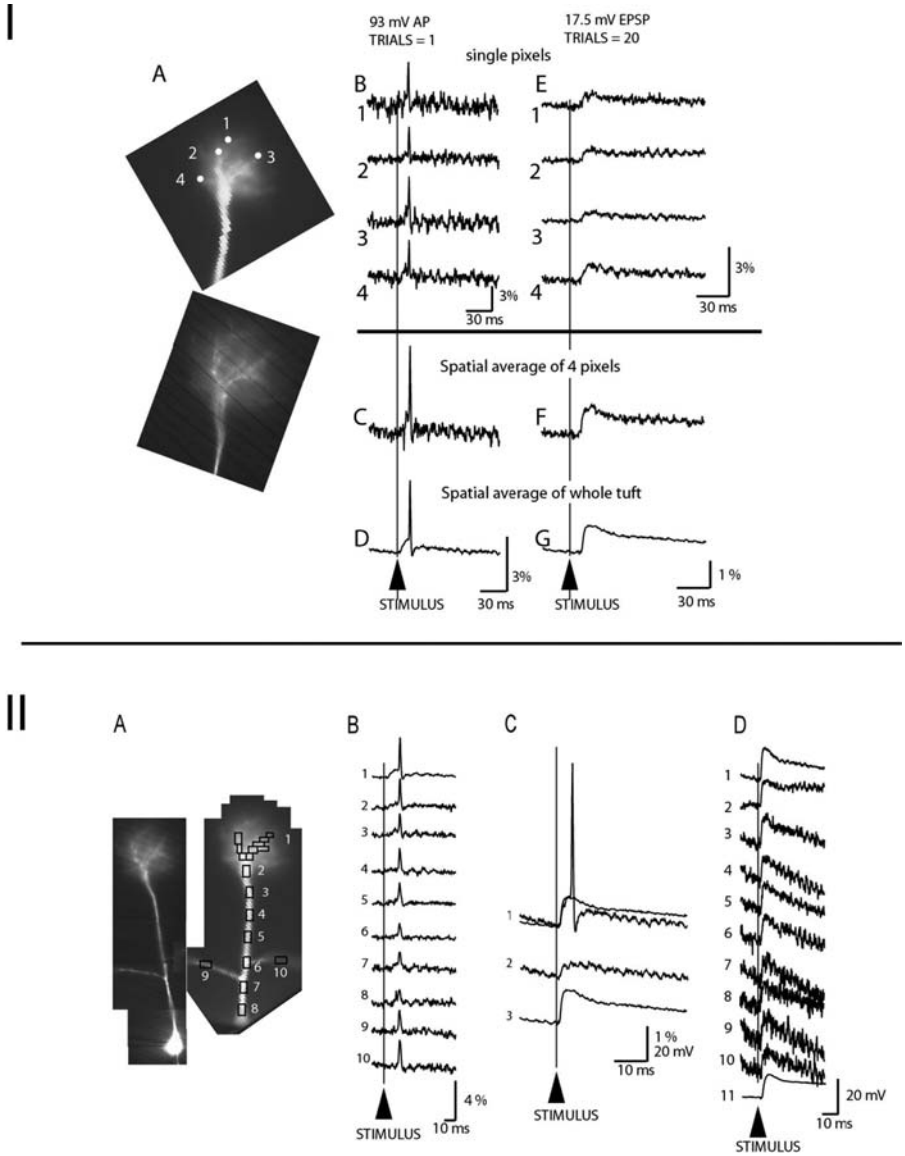

Fig. 3.4. Spatial resolution and sensitivity of voltage-imaging from neuronal processes. (**I**) (**A**) Low resolution (*upper*) and high resolution (*lower*) image of the terminal dendritic tuft. (**B**) Recordings of action potential signals from 4 individual pixels/locations on the dendritic tuft in single-trial measurements (no averaging). (**C**) The signal-to-noise ratio with spatial averaging of 4 pixels/locations from B. (**D**) The signal-to-noise ratio with spatial averaging of the entire tuft area. (**E**) An evoked EPSP recorded from 4 individual locations on the dendritic tuft; 20 trials averaged. (**F**) Spatial average of 4 pixels shown in E. (**G**) Spatial average of the entire tuft area. (**II**) Attenuation of the EPSP along the primary dendrite. (**A**) High and low resolution image of a mitral cell. (**B**) Single-trial optical recordings of action potential signals from ten different regions on the primary and oblique dendrites. The rectangles indicate pixels that were averaged to obtain traces 1–10. The amplitude of the action potential measured from the soma by a patch-electrode was 93 mV (resting potential-to-peak). The amplitude of optical signals ($\triangle F/F$) corresponding to a spike of constant size varied with the location *(1–10)* due to unequal sensitivity of the optical measurement from different locations. The sensitivity profile, determined from action potential measurements, provides a calibration for the conversion of optical signals to membrane potential changes. In the measurements shown, the calibration factors (from the tuft to the most proximal part of the primary dendrite) are: 1; 0.74; 0.56; 0.63; 0.53; 0.38; 0.40; 0.32 and 0.47 for the left and 0.59 for the right oblique

The images of the dendritic tuft of a mitral cell (upper image – low resolution; lower image – high resolution) are shown in (A). Single pixel recordings of action potential signals from four individual locations on the dendritic tuft in single-trial measurements (no averaging) are shown in B. Action potential signals from individual locations could easily be resolved. An improvement in the signal-to-noise ratio with minimal spatial averaging (signals from the four pixels shown in B is illustrated in panel C). A dramatic improvement with more extensive spatial averaging (the whole tuft; 184 pixels) made the optical recording shown in D appear similar in signal-to-noise ratio to electrode measurements. Measurements of the same type were carried out during an evoked synaptic potential at the dendritic tuft (**Fig. 3.4-I, E, F and G**). Because excitatory post-synaptic potential (EPSP) was about 5 times smaller in amplitude than an action potential, we averaged 20 individual trials to obtain a signal-to-noise ratio similar to the one corresponding to action potentials (the signal-to-noise ratio increases with the square root of the number of averages). Panels E, F and G of **Figure 3.4-I** again illustrate the striking improvement in the sensitivity of recording with both spatial averaging and averaging of individual repetitive events. This sensitivity was routinely obtained from mitral cells that were positioned relatively close to the surface of the slice (not deeper than 70 μm) and that had its primary dendrite and tuft close to the focal plane.

Figure 3.4-II illustrates a representative example from a series of optical measurements designed to determine the characteristics of the evoked EPSP at the site of origin and its attenuation along the primary dendrite. This information was not possible to obtain before using electrode measurements because of the small diameter of terminal dendritic branches. First, a spike was elicited and optically recorded from multiple sites in a single-trial measurement to serve as a calibration standard (**Fig. 3.4-II B**, traces 1–10). The calibration of optical data from multiple sites in terms of membrane potential requires a voltage

Fig. 3.4. (continued) branch. (**C**) Calibration of optical signals (ΔF/F) in terms of membrane potential (mV). All traces represent the average output of the same group of 35 pixels that receive light from the dendritic tuft (rectangles over the tuft in A). Twenty trials were averaged to improve the signal-to-noise ratio. Trace 1 shows an optical signal corresponding to an action potential of 93 mV used as a calibration standard. Trace 2 is a subthreshold EPSP signal evoked by olfactory nerve stimulation and calibrated to be 9 mV in amplitude at the site of origin (tuft). Trace 3 shows a threshold EPSP signal recorded from the tuft after the action potential was blocked by intracellular application of QX-314. In the measurement shown in trace 3, the stimulus delivered to the olfactory nerve was identical to the one applied in the measurement shown in trace 1. The EPSP signal in trace 3 (also superimposed over trace1) overlaps closely with the local response preceding a spike in trace 1 indicating that the spike is eliminated by QX-314 while the synaptic potential was unchanged. (**D**) The amplitude of EPSP signals on a voltage scale at 10 recording sites. The calibration of optical signals shows that EPSP at location 8, only 15 μm away from soma, is 13.2 mV in amplitude. Electrical recording from the soma (trace 11 in (**D**)) was similar (12.5 mV). Traces *(9, 10)* are signals from left and right oblique dendritic branches.

signal that has a known amplitude at all recording locations on neuronal processes *(29)*. In a general case, such a signal is not available. However, the action potential amplitude in mitral cells is constant along the entire length of the primary dendrite, as established by direct electrical measurements *(30–32)* and, thus, can be used as a calibration signal.

A typical threshold EPSP recorded from the dendritic tuft is shown in **Fig. 3.4-II** C. Trace 1 shows the EPSP that was suprathreshold for spike initiation in the control solution and an EPSP alone after spike was blocked with QX-314 to facilitate averaging synaptic potentials. The amplitude and the shape of the EPSP were mostly unaltered by the drug. The EPSP was monitored optically and calibrated in terms of membrane potential along a 260 μm primary dendrite. The optical signals are shown on a voltage scale in **Fig. 3.4-II** D. The recordings from 8 locations on the primary dendrite (traces 1–8), including the terminal tuft, and two sites on oblique dendrites (traces 9 and 10) are shown together with the electrical recording from the soma (trace 11). The calibration of the EPSP in the tuft revealed that the peak amplitude was 18 mV. The EPSP amplitude in the soma, determined from optical data, was 13.2 mV (panel D, trace 8). The direct electrical recording of the EPSP in the soma (panel D, trace 11) showed amplitude of 12.5 mV. This result indicates that the error in calibrating optical signals can be very small. A series of measurements of this type provided information about the characteristics of the EPSPs at the synaptic sites and its attenuation along the primary dendrite. On average, the EPSP attenuated by $35 \pm 9\%$ in 300 μm. The mean apparent "length constant" in the primary dendrites of mitral cells was unusually long, corresponding to approximately 1200 μm *(24)*.

It is often useful to monitor and correlate regional dendritic membrane potential signals and the associated local calcium transient, the two signaling pathways that control a variety of functions in individual neurons. We combined voltage imaging and Ca^{2+} imaging from the dendritic arbor of individual neurons loaded with two indicators. In this approach, changes in membrane potential and in $[Ca^{2+}]i$ are recorded sequentially from the dendritic tree of the same neuron as fractional changes in fluorescence intensity using two different filter sets *(12)*. **Figure 3.5** is an example of typical measurements carried out to correlate *V*m signals with corresponding changes in $[Ca^{2+}]_i$ during the EPSP–AP pairing protocol that typically induces long-term potentiation (LTP) in hippocampal CA1 pyramidal neurons. *V*m signals and $[Ca^{2+}]i$ transients were monitored during three stimulation protocols (APs alone, EPSPs alone, paired stimulation) from multiple sites on a dendritic tree. The recordings from one location on an oblique dendrite close to a stimulating electrode revealed a marked localized supralinear increase in the $[Ca^{2+}]_i$ signal evoked by pairing a train of EPSPs with a burst of two backpropagated

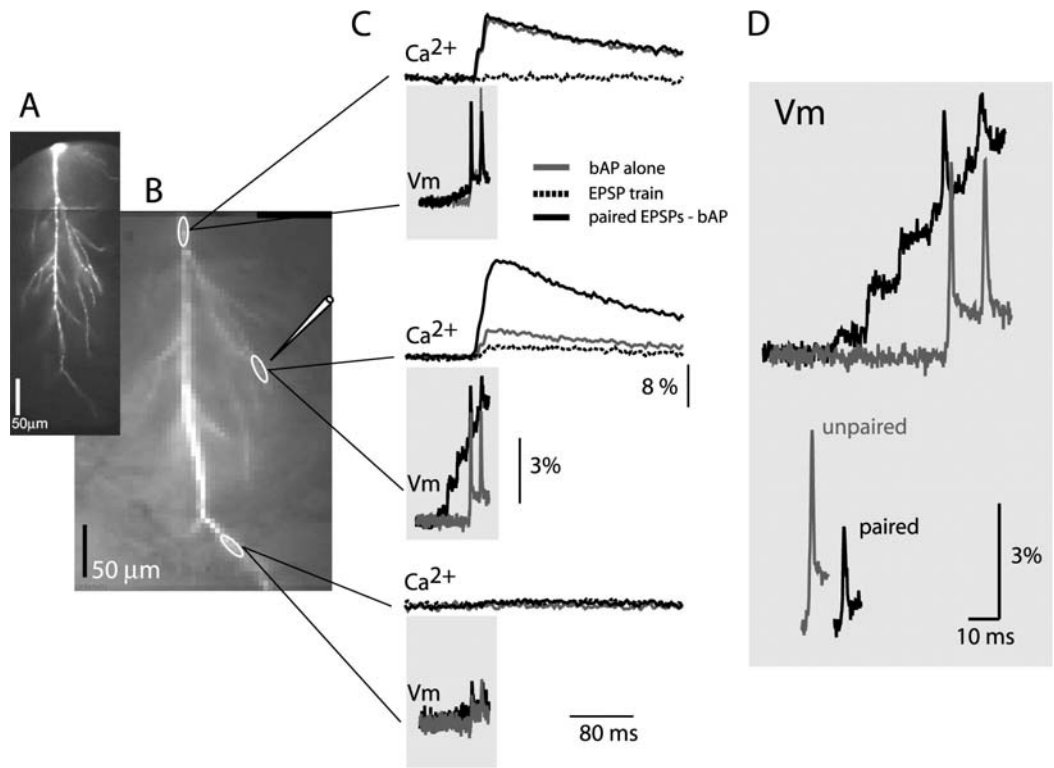

Fig. 3.5. Comparison of *V*m and $[Ca^{2+}]_i$ signals from same dendritic locations. (**A**) A composite image of a neuron (voltage-sensitive dye excitation). (**B**) Low resolution images (bis-fura-2 excitation) of the dendritic arbor in recording position. Representative recording locations marked by white ovals; the position of the extracellular electrode shown schematically. (**C**) Vm signals and $[Ca^{2+}]_i$ signals related to backpropagated action potentials (bAP, gray traces), EPSP train (dashed traces, shown only for $[Ca^{2+}]_i$ signals), and paired EPSP–AP activity (dark traces). Vm signals (100 ms) during paired activity are superimposed with the recordings of bAP signals alone. Calcium recordings (400 ms) are shown above Vm traces – signals during three stimulation protocols (bAPs, EPSP train, paired) are superimposed. (**D**) Vm recordings of bAPs on the expanded time scale superimposed on the same baseline to show region-specific changes in the peak membrane depolarization during paired activity (upper traces). Traces are shifted horizontally with respect to each other for clarity. Lower traces: The first spike signals (unpaired and paired) aligned to indicate the difference in baseline-to-peak amplitude (EPSP signal subtracted).

APs (**Fig. 3.5C**; middle set of traces). At the same time, a dramatic reduction in the baseline-to-peak local AP amplitude was observed during the paired stimulation. The reduction in the size of the backpropagated AP during paired activity is illustrated in **Fig. 3.5D**. The spike signals corresponding to backpropagated APs evoked alone and during paired activity are superimposed on the baseline membrane potential before the EPSP train (upper traces) and on the baseline membrane potential immediately preceding the spikes evoked during the last two EPSPs in a train (lower traces). Clearly, a supralinear increase in $[Ca^{2+}]_i$ that serves as a trigger for LTP induction did not require boosting in bAP baseline-to-peak amplitude. This initial result was followed by a series of experiments carried out to characterize the relationship between electrical signals and related $[Ca^{2+}]_i$ transients during

EPSP-AP pairing activity pattern that induces persistent changes in synaptic efficacy *(12)*.

2.2. Activity of Many Individual Neurons in the Mouse Primary Somatosensory/Visual Cortex in Response to Sensory Stimulation (Fig. 3.3, Middle Panel)

Nervous systems are made up of large numbers of neurons and, many of these are active during the generation of behaviors. The original motivation for developing optical methods for monitoring activity was the hope that they could be used to record activity of many neurons simultaneously during behaviors *(33)*. Obtaining information about the activity of many cells is essential for understanding the roles of the individual neurons in generating behavior and for understanding how nervous systems are organized.

One simple and widely used method to monitor neuronal activity relies on imaging the neuron's intracellular Ca^{2+} concentration. Indeed, in living cells, most depolarizing electrical signals are associated with Ca^{2+} influx caused by the activation of different types of voltage-gated Ca^{2+} channels, abundantly expressed in the nervous system *(34, 35)*. Such signals are often further amplified by Ca^{2+} release from intracellular Ca^{2+} stores *(36)*. The easiest technique to monitor activity of many individual neurons by imaging their intracellular Ca^{2+}concentration uses a membrane permeant acetoxymethyl (AM) ester form of a Ca^{2+} indicator dye. Such dyes were first introduced by R.Y. Tsien *(37)* and widely used ever since. For the vertebrate brain in vivo, the method allowing imaging of neural ensembles with single cell resolution was introduced by Stosiek et al. *(38)*. The technique was originally developed for imaging layer 2/3 neurons in the mouse cortex (**Fig. 3.6**), and was successfully applied later to stain dif-

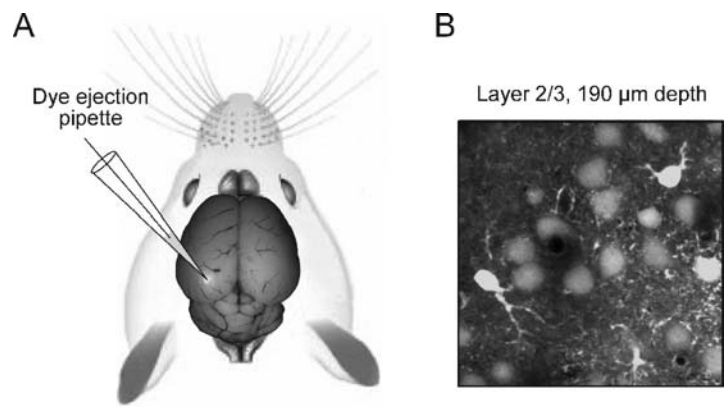

Fig. 3.6. A, a schematic drawing illustrating in vivo multi cell bolus loading of cortical neurons with a calcium indicator dye. The membrane-permeant dye is pressure-injected from the patch pipette into the extracellular space. Subsequently, it diffuses into the cells where it is deesterified by intracellular esterases. B, an example of image quality. The cells in layer 2/3 of the primary visual cortex were stained using multi cell bolus loading and visualized using two-photon imaging.

ferent neuronal tissues in a variety of species from lower vertebrates to mammals *(39–45)*. This technique utilizes a "bolus" injection of a membrane-permeant Ca^{2+} indicator dye into the extracellular space. Briefly, a pipette containing the AM form of an indicator dye is inserted into the tissue of interest and approximately 400 fl of the dye-containing solution is pressure-ejected at the desired depth. We typically use patch-like pipettes with a pipette resistance of 6–9 MOhm when filled with the pipette solution *(38)*. For the detailed step-by-step description of the technique (including the list of required equipment as well as tip and troubleshooting table), we refer the reader to Garaschuk et al. *(112)*. When injected into the brain parenchyma, the dye diffuses into the cells of interest where it is hydrolyzed by intracellular esterases. The remaining dye is rapidly removed from the extracellular space by microcirculation *(46)*. The technique accommodates any AM indicator dye of interest (also Ca^{2+} insensitive dyes like, for example, Calcein AM). Ca^{2+}indicator dyes successfully used so far include: Fura-2 AM, Fura-PE3 AM, Fura Red AM, Indo-1 AM, Calcium Green-1 AM, Oregon Green 488 BAPTA-1 AM, Fluo-4 AM, and Magnesium Green AM.

2.2.1. Example Results

Figure 3.7 illustrates Ca^{2+} transients evoked in layer 2/3 cortical neurons in response to sensory stimulation. In **A**, neurons in the barrel cortex were activated by the air-puff induced movement of the majority of whiskers on the contralateral side of the mouse's snout. In **B**, cells in the primary visual cortex were activated by repetitive light flashes. Note that not all cells in **B** are responding to this kind of stimulus (compare cells 1, 4 with cells 2, 3). The figure also illustrates two different approaches used for recording stimulus-induced Ca^{2+} transients. In **A**, Ca^{2+} transients were recorded at 200 Hz sampling rate using line scan mode. While providing "real time" temporal resolution, this technique reduces the spatial dimension of the recordings to a single line (*scan line* in **A**). In **B**, the area containing 4 neighboring neurons was imaged at frame rate of ~20 Hz. Note that although the individual cell bodies can be clearly distinguished, the multi cell bolus loading technique does not provide imaging contrast sufficient to resolve individual dendritic processes.

2.3. Population Signals from Olfactory Receptor Neuron Terminals in the Olfactory Bulb Glomeruli (Fig. 3.3, Right Panel)

A very large number (~10,000) of olfactory receptor neurons send their axons to each glomerulus in the olfactory bulb. These nerve terminals are small, ~1 μm in diameter, far below the spatial resolution obtainable using wide-field microscopy. Thus, wide-field imaging from the glomerulus will result in a population signal, a signal that is the population average of what is happening in all 10,000 terminals. Selective labeling of olfactory receptor neuron nerve terminals with a calcium-sensitive dye was used to visualize the spatial-temporal patterns in the input from the nose to

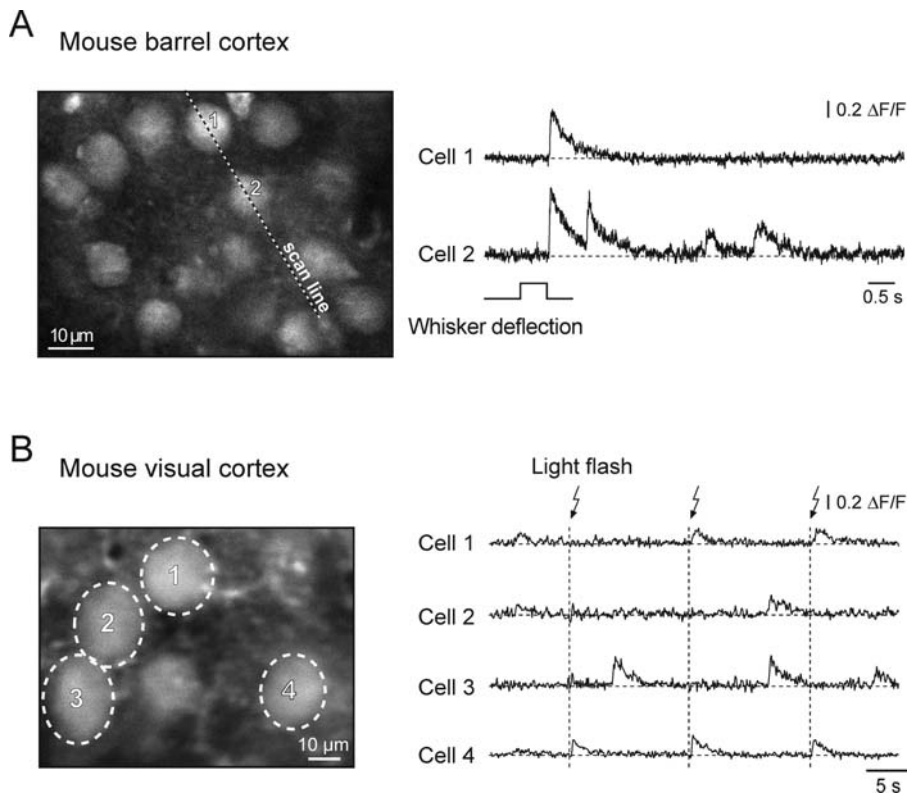

Fig. 3.7. Sensory-driven Ca^{2+} transients in individual cortical neurons. A, individual neurons in the mouse barrel cortex (*left*) and the corresponding Ca^{2+} transients (*right*) evoked by whisker deflection. Whiskers at the contralateral side of the snout were moved by air puffs. The transients were recorded using the line-scan mode (5 ms/line; the position of the scanned line is indicated). B, individual neurons in the mouse visual cortex (*left*) and the corresponding Ca^{2+} transients (*right*) evoked by brief consecutive light flashes. A is reproduced, with permission from National Academy of Sciences USA, copyright 2003, from Stosiek et al. *(38)*, B is reproduced, with permission from Springer-Verlag copyright 2006 from Garaschuk et al. *(112)*.

the dorsal surface of the olfactory bulb. This area encompassed approximately 150 glomeruli. While functional imaging methods such as fMRI, 2-deoxyglucose, and intrinsic imaging reveal patterns of glomerular activity (e.g., *(47–49)*), with these methods, it is difficult to determine whether the signals come from presynaptic terminals and/or from post-synaptic juxtaglomerular and/or mitral/tufted processes in the glomerulus. In selected instances, labeling neurons with voltage- or calcium-sensitive dyes via retrograde or anterograde transport allows selective monitoring of activity in defined neuronal populations (e.g., *(50–52)*). This approach was first developed for the olfactory receptor neurons by Friedrich and Korsching *(53)* in the zebrafish and later adapted for use in the mouse *(54)*.

2.3.1. Dye Screening

We tested one calcium-sensitive dye, Calcium Green-1 (Invitrogen-Molecular Probes, Eugene OR), that was not dextran conjugated. While it did label receptor neurons in the

olfactory epithelium, we did not detect labeling in the neuron terminals in the olfactory bulb. Thus, our choice of calcium dyes was limited to those that can be obtained as dextran conjugates. We tried both Calcium Green-1 dextran and Fluo-4-dextran *(51)*. In our hands, labeling was more reliable and the fluorescence signals were larger with Calcium Green-1 dextran. We tested both the 3,000 kD and the 10,000 kD dextran conjugates of Calcium Green-1. No clear difference was observed. Yaksi and Friedrich *(55)* used rhod-dextran but noted that the signal-to-noise ratio was lower than that obtained with the green calcium indicators.

2.3.2. Methods for the In Vivo Mouse Preparation

Because dextran-conjugated dyes are membrane impermeant, loading olfactory receptor neurons with Calcium Green-1 dextran requires treatment with a permeabilizing agent. Friedrich and Korsching *(53)* found that coapplication of Calcium Green-1 dextran with a dilute solution of Triton-X 100 detergent was an effective method for loading zebrafish olfactory receptor neurons.

For imaging, mice were anesthetized with pentobarbital (50 mg/kg, i.p.). A double tracheotomy was performed so that an artificial sniff paradigm using the upper tracheotomy tube allowed for precise control of odorant access to the nasal cavity. This helped to ensure a fixed and rapid onset of the signal which was important when multiple trials were averaged. The mice breathed freely through the lower tracheotomy tube. The dorsal surface of one olfactory bulb was illuminated with 480±25 nm light using a 150 W Xenon arc lamp and 515 nm long-pass dichroic mirror, and fluorescence emission above 530 nm was collected (**Fig. 3.8**, right panel). Images were acquired and digitized with an 80×80 or 256×256 pixel CCD camera (NeuroCCD-SM or NeuroCCD-SM256; RedShirtImaging LLC, Decatur, GA) and stored on disk at a 25 or 32.25 Hz frame rate. Fluorescence was imaged using a 10.5×, 0.2 N.A. objective (spatial resolution, 20 μm per pixel assuming no scattering or out-of-focus signals) or a 14×, 0.4 N.A. objective (15 μm per pixel resolution). The olfactometer *(56)* was an improved version of the one used in Lam et al. *(57)*.

While odorant-evoked signals were detected in single trials (e.g. **Fig. 3.9C**), we typically collected, then averaged, responses of two to eight consecutive odorant presentations in order to improve the signal-to-noise ratio and to obtain a measure of trial-to-trial variability. To avoid habituating the response, we waited a minimum of 60 s between trials. The primary source of extrinsic noise was movement associated with respiration and heartbeat. The noise was largest in regions adjacent to major blood vessels, and so pixels overlying these regions were sometimes removed from the data set (omitted) prior to analysis. Occasional trials with widespread artifactual signals (primarily due to movement) were

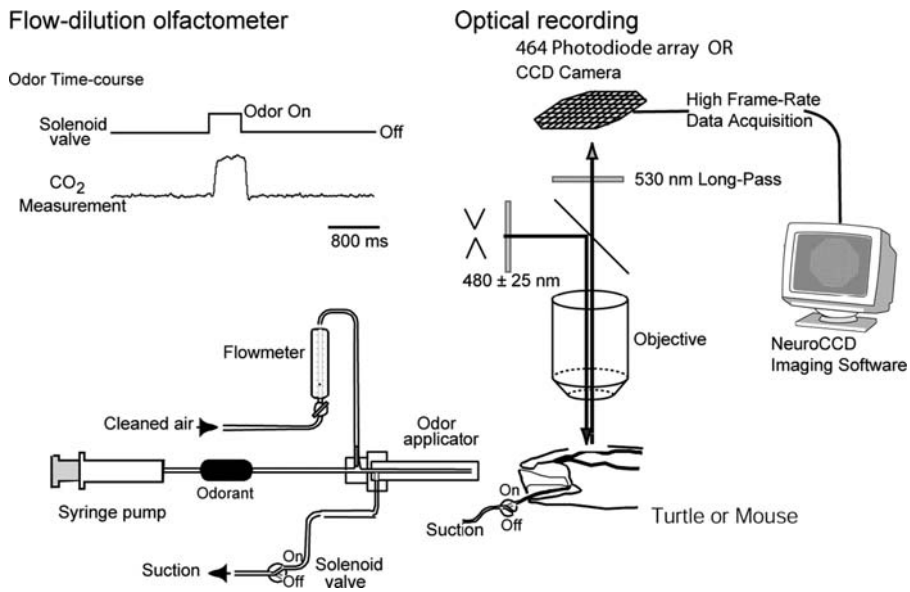

Fig. 3.8. *Left Panel*: *Top*: Time course of the odor output from the olfactometer measured by monitoring the CO_2 in the carrier gas. The upper trace shows the time-course of the command pulse delivered to the suction solenoid of the outer barrel of the odor applicator. The lower trace is the output of the CO_2 detector probe. There is a delay of about 100 ms between the command pulse and the arrival of the pulse at the CO_2 detector. The odor-pulse is approximately square shaped. *Bottom*: Schematic diagram of the olfactometer. Compressed air was cleaned, hydrated and then mixed with room air saturated with odorant vapor in the odor applicator. The flow rates of the air and the odorant vapor were controlled by a flow-meter and a syringe pump respectively. The odor-applicator had two barrels; the outer one was normally under suction to remove the odor. Turning-off of the suction to the outer barrel releases odorant from the end of the applicator. *Right Panel*: Schematic diagram of the optical imaging apparatus. The olfactory bulb was illuminated using a 100 W tungsten halogen lamp or a xenon arc lamp. The incident light passed through a heat filter and a 480 $\pm$ 30 nm band-pass interference filter and was reflected onto the preparation by a long-pass dichroic mirror (510 nm). The image of the preparation was formed by a 10.5$\times$ or 14$\times$ objective lens onto an 80$\times$80 CCD camera after passing through a 530 nm long-pass secondary filter. The secondary filter is needed to block reflected incident wavelengths that are transmitted by the dichroic mirror. (D. Vucinic, L. B. Cohen, S. Kosmidis, unpublished.)

discarded. After averaging, data from each pixel were temporally filtered with a 1–2 Hz low-pass Gaussian and a 0.017 Hz high-pass digital RC filter.

To correct for unequal labeling of glomeruli, the signal from each pixel was divided by its resting fluorescence obtained at the beginning of each trial. A significant part of the resting fluorescence arises from dye in axons running along the surface of the bulb prior to entering in glomeruli. Because there is no detected increase in calcium in axons *(58)*, this correction is only partially successful. To construct the spatial maps of input to the bulb, response amplitudes for each pixel were measured by subtracting the temporal average of frames in a time window just preceding the stimulus from a temporal average centered at approximately the peak of the response.

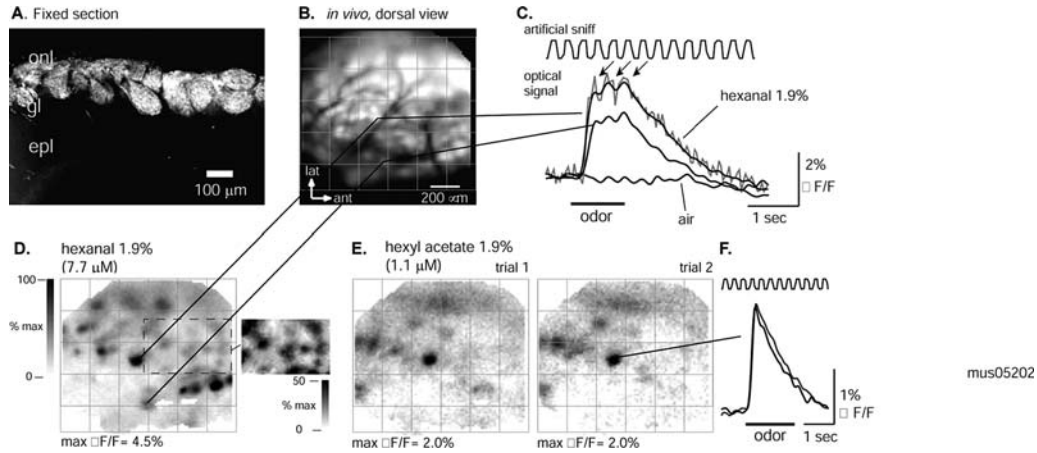

Fig. 3.9. Imaging mouse olfactory receptor neuron activation after in vivo loading with Calcium Green-1 dextran. (**A**) Confocal image of a section through one olfactory bulb fixed 5 days after loading. Fixable rhodamine dextran (10 kD) was used instead of Calcium Green dextran to preserve labeling in fixed tissue. Glomeruli are strongly labeled. There is no evidence of transsynaptic labeling. onl, olfactory nerve layer; gl, glomerular layer; epl, external plexiform layer. (**B**) Resting Calcium Green-1 dextran fluorescence imaged in vivo, 7 days after loading. The image was contrast-enhanced to emphasize individual glomeruli. Blood vessels appear as dark lines. The saturated regions in the upper right are from olfactory nerve bundles that obscure underlying glomeruli. Lines originate from two glomeruli whose responses are shown in (**C**) and (**D**). (**C**) 1.9% hexanal evoked rapid (~200 ms rise-time) increases in fluorescence in the two glomeruli indicated in (**B**) (*lines*). Each trace shows the optical signal measured from one pixel and from a single trial after band-pass filtering from 0.017 to 2 Hz. (**D**) Gray-scale map of the evoked signal for the trial shown in (*C*), showing foci of fluorescence increases. A region of the map normalized to 50% of the maximum signal (*inset*) shows additional smaller-amplitude foci. (**E**) The spatial distribution and amplitude of the signals was consistent across repeated odorant presentations and was different for different odorants (D–E). Redrawn from Wachowiak and Cohen *(54)*.

2.3.3. Example Results

Calcium Green-1 dextran loading resulted in labeling of olfactory receptor axon terminals in the olfactory bulb (**Fig. 3.9A, B**). We imaged odorant responses from the dorsal olfactory bulb of anesthetized mice 4–8 days after loading. Odorant presentation evoked rapid (100–500 ms rise-time) increases in fluorescence of up to 9% $\Delta F/F$ (**Fig. 3.9C**). Spatial maps of the response amplitude measured from each pixel showed well-defined foci of fluorescence increases (**Fig. 3.9D**), often corresponding to individual glomeruli visible from the resting fluorescence (**Fig. 3.9B**). Odorant-evoked signals showed a range of amplitudes in different glomeruli. Using an expanded gray scale (**Fig. 3.9D**, inset), it is clear that even smaller signals have glomerular localization. The spatial distribution and amplitude of the signals were consistent across repeated odorant presentations (**Fig. 3.9E**) and were different for different odorants (**Fig. 3.9D–E**).

The noise in this measurement of fluorescence from transported dye is also consistent with expectations from a calculation of the shot-noise (see below). In measurements made at a frame rate of 100 Hz, the number of photoelectrons per pixel per millisecond was approximately 2×10^4. Because we digitally

low-pass filtered the data at 2 Hz, the effective sample period is 500 msec and thus the number of photons/sample period is 10^7. The shot noise in this measurement should then be approximately 3×10^{-4} of the resting intensity. Consistent with this prediction, the noise in the measurements shown in **Fig. 3.9C** is less than 2×10^{-3} of the resting intensity. In preliminary measurements, we found that the shot noise and noise from respiration and heart beat were similar in magnitude.

The spatial resolution shown in **Fig. 3.9**, D-E is on the order of 20 μm, far better than might have been anticipated from the measurements illustrated in **Fig. 3.12**. However, both factors that could contribute to blurring are minimized in the measurements shown in **Fig. 3.9**. First, scattering will be lower because the Calcium Green-1 dextran is only in the outer two layers of the olfactory bulb. Second, out-of-focus signals will be small because the glomerular layer is only 100 μm thick.

Because many (up to 50) maps of this sort can be obtained from each preparation, considerable information has been obtained about the input from the nose to the bulb. However, it remains a challenge to determine the map of the output of the bulb carried by the mitral/tufted cells. If both the input and the output were known, we would have a strong clue about the function of this first way station in processing olfactory information.

3. Methodological Considerations

The three examples given above involved fractional intensity changes and signal-to-noise ratios that are not large. To measure these signals, the noise in the measurements had to be a substantially smaller fraction of the resting intensity. In the sections that follow, some of the considerations necessary to achieve such a low noise are outlined.

3.1. Signal Type

Sometimes it is possible to decide in advance which kind of optical signal will give the best signal-to-noise ratio, but in other situations, an experimental comparison is necessary. The choice of signal type often depends on the optical characteristics of the preparation. Extrinsic birefringence signals are relatively large in preparations that, like axons, have a cylindrical shape and radial optic axis *(59)*. However, in preparations with spherical symmetry (e.g., cell soma), the birefringence signals in adjacent quadrants will cancel *(60)*. Thick preparations (e.g. mammalian cortex) also dictate the choice of signal. In this circumstance, transmitted light measurements are not easy (a subcortical implantation of a light guide would be necessary), and the small size of the absorption signals that are detected in reflected light *(59,61)* meant that fluorescence or reflectance would be optimal *(62)*. Fluorescence

signals have most often been used in monitoring membrane potential and calcium concentration from tissue-cultured neurons. Both fluorescence and absorption have been used in measurements from ganglia and brain slices. Fluorescence or reflectance has always been used in measurements from intact brains.

3.2. Amplitude of the Voltage or Calcium Change

Both the signals are often presented as a fractional intensity change ($\Delta I/I$). These signals give information about the time course of the potential or calcium concentration change but no direct information about the absolute magnitude. However, in some instances, approximate estimations can be obtained. For example, the size of the optical signal in response to a sensory stimulus can be compared to the size of the signal in response to an epileptic event *(62)*. Another approach is the use of ratiometric measurements at two independent wavelengths *(63, 64)*. However, to determine the amplitude of the voltage or calcium change from a ratio measurement, one must know the fraction of the fluorescence that results from dye in the expected location, i.e. bound to active *versus* inactive membranes for voltage-sensitive dyes, or dye free in the axoplasm *versus* dye bound to protein or in intracellular compartments for calcium dyes. These requirements are only approximately met in special circumstances. For voltage-sensitive dyes, the best calibration is an electrode measurement of membrane potential. One case where this was possible was described in the first example presented above.

4. Measuring Technology

4.1. Noise

4.1.1. Shot Noise

The limit of accuracy with which light can be measured is set by the shot noise arising from the statistical nature of photon emission and detection. Random fluctuations in the number of photons emitted (and measured) per unit time occur; the root-mean-square (RMS) deviation in the number emitted is the square root of the average number. In a shot noise limited measurement, the signal-to-noise ratio is directly proportional to the square root of the number of measured photons and inversely proportional to the square root of the bandwidth of the photodetection system *(65, 66)*. The basis for the square root dependence on intensity is illustrated in **Figure 3.10**. In 10A, the result of using a random number table to distribute 20 photons into 20 time windows is shown. In 10B, the same procedure was used to distribute 200 photons into the same 20 bins. Relative to the average light level, there is more noise in the top trace (20 photons) than in the bottom trace (200 photons). On the right side of **Fig. 3.10**, the measured signal-to-noise ratios are listed; the improvement from

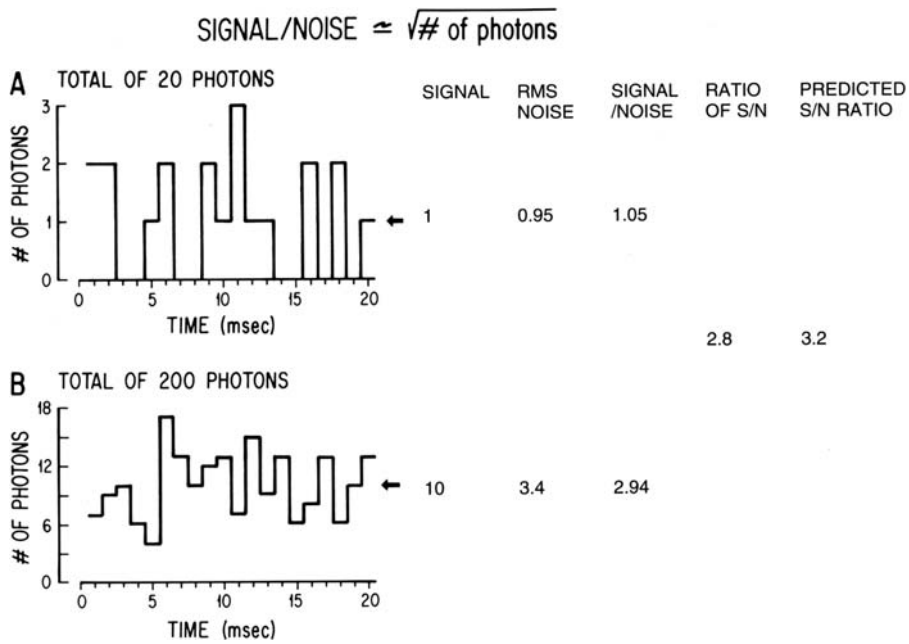

Fig. 3.10. Plots of the results of using a table of random numbers to distribute 20 photons (*top*, **A**) or 200 photons (*bottom*, **B**) into 20 time bins. The result illustrates the fact that when more photons are measured, the signal-to-noise ratio is improved. On the right, the signal-to-noise ratio is measured for the two results. The ratio of the two signal-to-noise ratios was 0.43. This is close to the ratio predicted by the relationship that the signal-to-noise ratio is proportional to the square root of the measured intensity.

A to B is similar to that expected from the square-root relationship. This square-root relationship is indicated by the dotted line in **Fig. 3.11** which plots the light intensity divided by the noise in the measurement versus the light intensity. In a shot-noise limited measurement, improvement in the signal-to-noise ratio can only be obtained by (i). Increasing the illumination intensity. (ii) Improving the light-gathering efficiency of the measuring system or (iii) Reducing the bandwidth.

4.1.1.1. The Optimum Signal to Noise Ratio in a Wide-Field Measurement

A tungsten filament lamp emits an average of 10^{16} photons/ms and the root-mean-square (RMS) deviation in the number emitted is the square root of this number or 10^8 photons/ms. However, because only a small fraction of the photons will be measured, a signal-to-noise ratio of 10^8 (see above) cannot be achieved. A partial listing of the light losses follows. A 0.9-NA lamp collector lens would collect 0.1 of the light emitted by the source. Only 0.2 of that light is in the visible wavelength range; the remainder is infrared (heat). Limiting the incident wavelengths to those which have the signal means that only 0.1 of the visible light is used. Thus, the light reaching the preparation might typically be reduced to 10^{13} photons/ms. If the light-collecting system that forms the image has high efficiency e.g., in an absorption measurement with matched condenser and

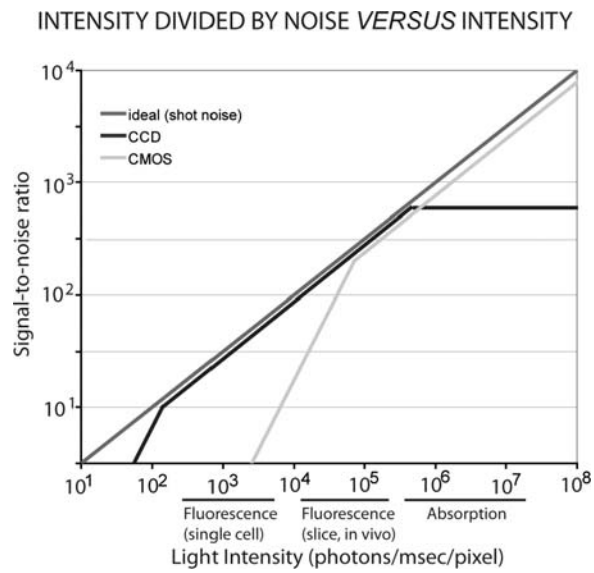

Fig. 3.11. The ratio of light intensity divided by the noise in the measurement as a function of light intensity in photons/ms/pixel. The theoretical optimum signal-to-noise ratio (medium line) is the shot-noise limit. Two camera systems are shown, a 10 kHz frame rate, 128×128 pixel, CMOS camera and a back-illuminated, 2 kHz frame rate, 80×80 pixel, CCD camera. The CMOS camera (*light line*) provides a near optimal signal-to-noise ratio at higher light intensities while the CCD camera (*dark line*) is better at lower intensities. The approximate light intensity per detector in fluorescence measurements from a single neuron, fluorescence measurements from a slice or in vivo preparation, and in absorption measurements from a ganglion or a slice is indicated along the x axis. The signal-to-noise ratio for the CMOS camera falls away from the ideal at low intensities because of dark noise. The lower dark noise of the cooled CCD allows it to function at the shot-noise limit at lower intensities until read noise dominates at about 10^2 photons/pixel/msec. The CCD camera saturates at intensities above 5×10^5 photons/ms/pixel.

objective numerical apertures, about 10^{13} photons/ms will reach the image plane. (In a fluorescence measurement, there will be much less light measured because 1. only a fraction of the incident photons are absorbed by the fluorophores, 2. only a fraction of the absorbed photons appear as emitted photons, and 3. only a fraction of the emitted photons are collected by the objective.) If the camera has a quantum efficiency of 1.0, then, in absorption, a total of 10^{13} photoelectrons/ms will be measured. With a camera of 10,000 pixels, there will be 10^9 photoelectrons/ms/pixel. The shot noise will be $10^{4.5}$ photoelectrons/ms/pixel; thus, the very best that can be expected is a noise that is $10^{-4.5}$ of the resting light (a signal-to-noise ratio of ~90 db). The extra light losses in a fluorescence measurement would further reduce the maximum obtainable signal-to-noise ratio.

One way to compare the performance of different camera systems for wide-field imaging and to understand their deviations from optimal (shot-noise limited) is to determine the light

intensity divided by the noise in the measurement and plot that versus the number of photons reaching each pixel of the camera. The dotted line in **Fig. 3.11** is the plot for an ideal camera. At high light intensities, this ratio is large and thus small changes in intensity can be detected. For example, at 10^{10} photons/ms, a fractional intensity change of 0.1% can be measured with a signal-to-noise ratio of 100. On the other hand, at low intensities, the ratio of intensity divided by noise is small and only large signals can be detected. For example, at 10^4 photons/msec, the same fractional change of 0.1% can be measured with a signal-to-noise ratio of 1 only after averaging 100 trials.

In addition, **Fig. 3.11** compares the performance of two particular camera systems, a CMOS camera (solid lines) and a back-illuminated cooled CCD camera (dashed lines), with the shot noise ideal. A 128×128 pixel CMOS camera approaches the shot-noise limitation over the range of intensities from 10^5 to 10^9 photons/ms/pixel. This is the range of intensities obtained in absorption measurements and fluorescence measurements using bath applied dye on in vitro slices and intact brains. On the other hand, the cooled 80×80 pixel CCD camera approaches the shot noise limit over the range of intensities from 10^2 to 5×10^5 photons/ms. This is the range of intensities obtained from fluorescence experiments on individual cells and neurons. In the discussion that follows, we will indicate the aspects of the measurements and the characteristics of the two camera systems which cause them to deviate from the shot noise ideal. The two camera systems we have used to illustrate in **Fig. 3.11** have excellent dark noise and saturation characteristics; other cameras would be dark noise limited at higher light intensities and would saturate at lower intensities.

4.1.1.2. The Optimum Signal-to-Noise Ratio in Two-Photon Scanning Microscopy Measurements

Similar considerations apply to two-photon measurements. Because two-photon excitation will only occur with the nearly synchronous arrival of two low-energy photons, excitation is proportional to the square of light intensity and only very high intensity sources achieve significant excitation. In practice, this restricts the light source to pulsed lasers with very narrow pulses. In the experiments illustrated in Example 2 (above), the laser intensity was not limiting because the targeted cells were only some 150–250 μm below the surface of the preparation and losses in focal intensity from light scattering were not large. For cells as deep as mitral cells (~400 μm below the surface), the loss of the excitation light due to photon dispersion within the tissue becomes significant. In addition, in the neural tissue, the quality of in-depth imaging often suffers from (i) inhomogeneity of the refractive indices within the tissue (e.g. blood vessels, clusters of cell bodies acting as microlenses *(67)*), (ii) light absorption by the hemoglobin, (iii) generation of out-of-focus fluorescence

while increasing laser power etc. For a thorough description of approaches used to improve the imaging depth as well as image quality, we refer the reader to the recent review of Helmchen and Denk *(67)*.

4.1.2. Extraneous (Technical) Noise

A second type of noise, termed extraneous or technical noise, is more apparent at high light intensities or at high spatial resolution. At high light intensities, the sensitivity to extraneous noise is high because the fractional shot noise and dark noise are low. One type of extraneous noise is caused by fluctuations in the output of the light source (see below). Two other sources of extraneous noise are vibrations and movement of the preparation.

4.1.2.1. Vibrational Noise in Wide-Field Measurements

A number of precautions for reducing vibrational noise have been described *(68, 69)*. The pneumatic isolation mounts on many vibration isolation tables are more efficient in reducing vertical vibrations than in reducing horizontal movements. There has been a series of progressively more successful (and expensive) solutions for vibration problems. A simple and inexpensive remedy is air-filled, soft rubber tubes (Newport Corp, Irvine, CA). For more severe vibration problems, Minus K Technology (Inglewood, CA) sells vibration isolation tables with very low resonant frequencies. The Halcyonics Micro 60 (Menlo Park, CA) is an active (piezoelectric drivers) isolator and can defeat airborne vibrations as well as those transmitted through the "ground" (Brian Salzberg, personal communication). Nevertheless, it has been difficult to reduce vibrational noise to less than 10^{-5} of the total light. With this amount of vibrational noise, increases in measured intensity beyond 10^{10} photons/ms would not improve the signal-to-noise ratio. For this reason and because of well size limitations, the performance of the CMOS system reaches a ceiling (**Fig. 3.11**, solid line).

4.1.2.2. Vibrational Noise in Two-Photon Measurements

Using a Newport Corporation Research Grade vibration isolation table reduces the vibrational noise so that it is less than the shot noise.

4.1.2.3. Preparation Movement

Preparation movement is often the limiting noise factor in in vivo measurements. This is true in wide-field measurements because the light intensity can be relatively high, reducing the shot noise to a level that is smaller than the movement noise. It is true in two-photon measurements because the spatial resolution and contrast are high and thus the sensitivity to movement is also high. The movement artifacts in vivo usually consist of irregular movements of the entire animal (less of a problem in anesthetized preparations) as well as of heart beat- and breathing-related vibrations. The higher frequency vibrations are usually the result of heart beat pulsation and are more profound in regions with a high

density of blood vessels. The heart beat- and breathing-related artifacts significantly increase their amplitudes when the skull and the *dura mater* are removed. (The multi cell bolus loading technique does not require dura removal.) The stability of recordings also depends on the diameter of the craniotomy. Thus, openings larger than 1 mm in diameter are often accompanied by large movement artifacts occurring at the heart beat frequency. Under such circumstances, the vibration noise can be reduced by covering the skull opening with 2% agarose and a glass coverslip *(70)*.

4.1.3. Dark Noise/Read Noise

Dark noise will degrade the signal-to-noise ratio at low light levels.

4.1.3.1. Wide-Field Imaging

Because of its electronic characteristics and because it is cooled, the CCD camera dark noise is substantially lower than that of the CMOS system. The CCD camera has read noise of 10e-rms at 1 kfps, low in an absolute sense. The larger dark noise in the CMOS camera accounts for the fact that the break in the curve in **Fig. 3.11** is substantially to the right of the intensity where the CCD camera becomes read-noise limited (10^2 photons/pixel/msec).

4.1.3.2. Two-Photon Imaging

The dark noise of photomultipliers (anode dark current) critically depends on supply voltage. At low-to-medium supply voltages, anode dark current is relatively low, but it increases dramatically at high supply voltages (usually higher than 700–800 V). To minimize dark noise, it is therefore advisable to conduct measurements at lowest PMT gain (e.g. lowest supply voltage) provided that the preparation tolerates the required increase in the intensity of excitation light. As a rule-of-thumb, the illumination intensity has to be as high and the corresponding PMT gain as low as possible to provide recording conditions just below the dye bleaching threshold.

4.2. Light Sources

Three kinds of sources have been used. Tungsten filament lamps are a stable source, but their intensity is relatively low, particularly at wavelengths less than 480 nm. Arc lamps are somewhat less stable but can provide higher intensity. Laser illumination can provide even more intense illumination.

4.2.1. Wide-Field Imaging

4.2.2. Tungsten Filament Lamps

It is not difficult to provide a power supply stable enough so that the output of the bulb fluctuates by less than 1 part in 10^5. In absorption measurements, where the fractional changes in intensity are relatively small, only tungsten filament sources have been used. On the other hand, fluorescence measurements often have larger fractional changes that will better tolerate light sources with systematic noise, and the measured intensities

are lower, making improvements in signal-to-noise ratio from brighter sources attractive.

4.2.3. Arc Lamps

Cairn Research Ltd (Faversham, UK) provides xenon power supplies, lamp housings, and arc lamps with noise that is in the range of 1 part in 10^4. A 150 watt lamp yielded 2–3 times more light at 520 $\pm$ 45 nm than a tungsten filament bulb. The extra intensity is especially useful for fluorescence measurements from processes of single neurons where the light intensity is low and the dark noise is a problem. In that situation, the signal-to-noise ratio will improve linearly with intensity.

4.2.4. Lasers

Laser illumination can provide the highest illumination intensity but avoiding photodynamic damage requires careful attention to minimizing illumination duration. The interference from speckle noise can be eliminated by reducing the beam coherence (Dejan Zecevic and Thomas Knopfel, personal communication).

4.2.5. Two-Photon Imaging

Two-photon imaging requires the use of a specific type of light source, pulsed lasers. These lasers use either a Titanium- sapphire (Ti:Sapphire) or a Nd:YAG (neodymium-doped yttrium aluminium garnet) oscillator. The Ti:Sapphire lasers provide wide tuning range (from 690 to 1080 nm) whereas Nd:YAG lasers typically operate at a wavelength of 1064 nm (although they can be also made to lase at their non-principal wavelengths of 946, 1320 or 1123 nm). At present, mostly Ti:Sapphire lasers are used for two-photon imaging of living tissues *(67, 71, 72)*.

4.3. Optics

The need to maximize the number of measured photons has been a dominant factor in the choice of optical components. In wide-field epifluorescence, both the excitation light and the emitted light pass through the objective, and the intensity reaching the photodetector is proportional to the *fourth* power of numerical aperture *(73)*. In two-photon imaging, only the collection of emitted light is affected by numerical aperture and thus the intensity reaching the photodetector is proportional to the square of numerical aperture. Clearly, numerical aperture is an important consideration in the choice of lenses. However, direct comparison of the intensity reaching the image plane has shown that the light collecting efficiency of an objective is not completely determined by the stated magnification and NA. In wide-field imaging, differences of a factor of five between lenses of the same specification have been observed.

4.3.1. Numerical Aperture

4.3.2. Back-Aperture of the Objective

Because of the strong light scattering within living tissue, in vivo two-photon imaging critically depends on detection of scattered photons. Under this condition, the size of back aperture of the objective (but also the size of all other apertures within the

detection pathway) becomes important. Ideally, one would like to employ an objective with high NA, large field of view (low magnification) and large back aperture. Such objectives recently became available from different manufacturers (Olympus, Nikon, Zeiss, etc.).

4.3.3. Depth of Focus in Wide-Field Imaging

Salzberg et al. *(68)* determined the effective depth of focus for a 0.4 NA objective lens by recording an optical signal from a neuron when it was in focus and then moving the neuron out of focus by various distances. They found that the neuron had to be moved 300 μm out of focus to cause a 50% reduction in signal size. Using 0.5 NA optics, Kleinfeld and Delaney *(74)* found that 100 μm out of focus led to a reduction in signal size of 50%.

4.3.4. Light Scattering and Out-of-Focus Light in Wide-Field Imaging

Light scattering can limit the spatial resolution of an optical measurement. **Figure 3.12** illustrates the results of experiments carried out on tissue from the salamander olfactory bulb. The top section indicates that when no tissue is present, essentially all of the light (750 nm) from a small spot falls on one detector. The bottom section illustrates the result when a 500 μm-thick slice of olfactory bulb is present. The light from the small spot is spread to about 200 μm. Mammalian cortex appears to scatter more than the salamander olfactory bulb. Thus, light scattering will cause considerable blurring of signals in vertebrate preparations. Presumably, this effect will be more severe at lower wavelengths because scattering by nervous tissue is inversely related to wavelength squared *(75)*.

A second source of blurring is signal from regions that are out of focus. For example, if the active region is a cylinder (a column) perpendicular to the plane of focus, and the objective is focused at the middle of the cylinder, then the light from the focal plane will have the correct diameter at the image plane. However, the light from the regions above and below is out of focus and will have a diameter that is too large. The middle section of **Fig. 3.12** illustrates the effect of moving the small spot of light 500 μm out of focus. The light from the small spot is spread to about 200 μm. Thus, in preparations with considerable scattering or with out-of-focus signals, the actual spatial resolution is likely to be limited by the preparation and not by the number of pixels in the imaging device.

4.3.5. Confocal and Two-Photon Microscopes

The confocal microscope *(76)* substantially reduces both the scattered and out-of-focus light by using a pinhole in the detection pathway. Two-photon microscopes also reduce out-of-focus light as well as out-of-focus phototoxicity and photobleaching *(77)*. In this case, however, the excitation of the fluorophore is restricted to the focal plane. With both types of microscope, one can obtain

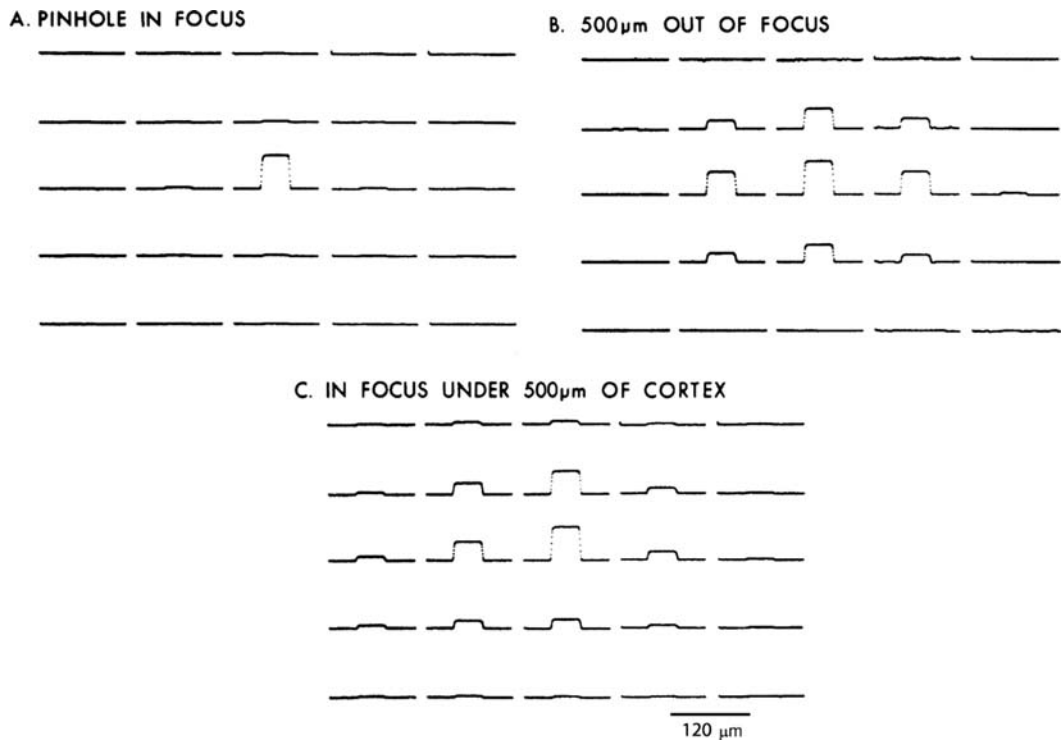

Fig. 3.12. Effects of focus and scattering on the distribution of light from a point source onto a camera. The data were acquired using a 464 element photodiode array. (**A**) A 40 μm pinhole in aluminum foil covered with saline was illuminated with light at 750 nm. The pinhole was in focus. More than 90% of the light fell on one detector. (**B**) The stage was moved downward by 500 μm. Light from the out-of-focus pinhole was now seen on several detectors. (**C**) The pinhole was in focus but covered by a 500 μm slice of salamander cortex. Again the light from the pinhole was spread over several detectors. A 10 × 0.4 NA objective was used. Kohler illumination was used before the pinhole was placed in the object plane. The recording gains were adjusted so the largest signal in each of the three trials would be approximately the same size in the figure. Redrawn from Orbach and Cohen *(61)*.

images from intact vertebrate preparations with much better spatial resolution than is achieved with wide-field microscopy. The two-photon microscope has been successfully used to monitor changes in calcium concentration inside small processes of neurons *(78)* and, in many individual cells, after bulk loading the AM ester calcium dyes (*(38)*; Example 2 above). Using a scanned line confocal microscope from Prairie Technologies (Middletown, WI), Jeff Magee and collaborators (personal communication) were able to measure voltage-sensitive dye signals from hippocampal cell dendrites at a frame rate of 3 kfps. Slower voltage-sensitive dye signals were measured confocally much earlier *(79)*.

4.4. Cameras

4.4.1. Quantum Efficiency

Because the signal-to-noise ratio in a shot noise limited measurement is proportional to the square root of the number of photons converted into photoelectrons, quantum efficiency is important. Silicon photodiodes and CCD and CMOS cameras can have quantum efficiencies approaching the ideal (1.0) at

wavelengths where most dyes absorb or emit light (500–900 nm). In contrast, only specially chosen vacuum photocathode devices (phototubes, photomultipliers, or image intensifiers) have a quantum efficiency as high as ~0.4. A relatively low fill factor and front illumination reduce the quantum efficiency of CMOS cameras to about 50%. This reduction will reduce the signal-to-noise ratio in a shot-noise limited measurement by a factor of about 1.4. Thus, in a low light level shot-noise limited situation, a CCD camera will have a larger signal-to-noise ratio. Photographic film has a much smaller quantum efficiency, <0.01 *(80)*.

4.4.2. EM-CCD Cameras

These cameras have on-chip multiplication and should lead to better signal-to-noise performance at very low light levels. However, the multiplication process adds noise (a factor of 1.4) and some existing chips are even noisier than expected from the factor of 1.4. If an ordinary CCD has a read noise of 10e-, then an ideal EM-CCD camera will have a better signal-to-noise ratio only at light levels less than 100 photons/pixel/frame. The light level achieved in the experiments illustrated in Example 1, where there is relatively little dye in small distal processes, is ~1000 photons/pixel/msec. Thus, in this measurement and all measurements with even higher light intensity, the CCD will have a better signal-to-noise ratio than an EM-CCD.

5. Future Directions

5.1. Organic Dyes

Because the light measuring apparatus is already reasonably optimized for all of the above applications, any improvement in sensitivity will need to come from the development of better dyes and/or investigating signals from additional optical properties of the dyes.

5.2. Organic Voltage-Sensitive Dyes

The voltage-sensitive dyes in **Fig. 3.2** and the vast majority of those synthesized are of the general class named polyenes *(81)*, a group that was first used to extend the wavelength response of photographic film. It is possible that improvements in signal size can be obtained with new polyene dyes (see *(4,5)* for a discussion of maximum possible fractional changes in absorption and fluorescence). On the other hand, the maximum fractional change has not increased in recent years (L. B. Cohen, A. Grinvald, K. Kamino, L. Loew, and B. M. Salzberg, personal communication), and most improvements (e.g. *(9, 25, 26, 51)*) have involved synthesizing analogues that work well on new preparations.

The best of the organic dyes have fluorescence changes of 10–20%/100 mv in situations where the staining is specific to

the membrane whose potential is changing *(26, 82, 83)*. Gonzalez and Tsien *(84)* introduced a new scheme for generating voltage-sensitive signals using two chromophores and fluorescence resonance energy transfer (FRET). While these fractional changes were also in the range of 10%/100 mv, more recent results are about 30% (Gonzalez and Tsien, personal communication). However, in order to achieve fast response times (> 100 Hz), one of the chromophores must be very hydrophobic and, as a result, does not penetrate into brain tissue. Thus far, it has not been possible to measure fast signals with a fast pair of dyes in intact tissues (Gonzalez and Tsien; Obaid and Salzberg; personal communication), although impressive results have been obtained where speed was not critical *(85, 86)*.

Membrane potential changes the non-linear second harmonic generation from styryl dyes *(87–89)*. Large (50%) fractional changes were measured. But, because the number of detected photons is small, the signal-to-noise ratios remain substantially smaller than that obtained with wide-field measurements.

5.3. Neuron-Type Specific Staining

An important new direction is the development of methods for neuron-type specific staining which would make it possible to determine the role of specific neuron types in generating the input-output function of a brain region. Three quite different approaches have been tried.

5.3.1. Directed Transport

The use of anterograde and retrograde dye transport has resulted in specific staining of olfactory receptor neuron terminals (Friedrich and Korsching *(53)*; Example 3) and motor neurons in embryonic chick and in lamprey spinal cords *(51)*. This method depends on finding a location where only one cell type is present that has a process leading to the brain area of interest. In lamprey experiments, spike signals from individual neurons were sometimes measured *(90)*. Further effort at optimizing this staining procedure is needed.

5.3.2. Staining Dependent on β-galactosidase Expression

The use of cell-type specific staining developed for fluorescein by Nirenberg and Cepko *(91)* might be extended to ion-sensitive or voltage-sensitive dyes.

5.3.3. Genetically Encoded Activity Sensors

5.3.3.1. Voltage Sensors

Siegel and Isacoff *(92)* constructed a genetically encoded combination of a potassium channel and green fluorescent protein. When expressed in a frog-oocyte, this molecule, FlaSh, had a (relatively slow; few hundred millisecond) voltage-dependent signal with a fractional fluorescence change of 5%. More recently, Ataka

and Pieribone *(93)* have developed a similar construct, SPARC, with very rapid kinetics. Unfortunately, in mammalian cells, both of these FP-voltage sensors are only minimally expressed in the extracellular membrane *(94)*. They appear to be retained in the endoplasmic reticulum. Thomas Knopfel and collaborators *(95)* investigated a new class of voltage- sensitive proteins, the voltage-sensitive phosphatase from *Ciona intestinalis (96)*. They replaced the phosphatase domain with a FRET pair and this protein, VSFP2.1, both trafficked well to the external membrane of hippocampal neurons and had a voltage-dependent response. VFSP2.1 was faster than FlaSh but slower than SPARC. Future efforts will be needed to improve the response time and signal size of VFSP2.1 and to test the construct in transgenic systems.

5.3.4. Calcium Sensors

There exists a rather large family of genetically encoded fluorescent Ca^{2+} indicator proteins. Until recently, all protein calcium sensors employed Ca^{2+} binding to calmodulin (CaM) and Ca^{2+}-dependent interaction of calmodulin and the CaM binding peptide M13 as a calcium sensor. The CaM-M13 complex was then attached to green fluorescent protein or one of its variants to generate a single-wavelength Ca^{2+} indicator *(97–102)*. Alternatively, the CaM-M13 complex was sandwiched between CFP (cyan fluorescent protein) and YFP (yellow fluorescent protein) to generate ratiometric Ca^{2+} sensors like the "Cameleons" *(103, 104)*. Calmodulin-based calcium sensors function well in invertebrates and lower vertebrates (for review see refs. in Miyawaki *(104)*), but show rather poor performance in mammals *(105–108)*. Significant improvement of protein calcium sensor performance in mammalian neurons came from the use of alternative Ca^{2+}-binding protein Troponin C (TnC; *(109–111)*). The members of the TnC family have relatively high dynamic range (4-fold increase in signal strength upon changing Ca^{2+} concentration from 0 to 10 mM), rather fast rise and decay times *(108)* and they respond linearly to an increase in Ca^{2+} concentration within the physiological activity range *(102, 111)*. TnC-based indicators can be expressed transgenically in mice and allow in vivo imaging of neural function with single-cell and even subcellular resolution *(111)*. While recent developments significantly improved the properties of protein calcium sensors, when compared to organic Ca^{2+} indicators, the protein sensors are still inferior when Ca^{2+} sensitivity and/or dynamic range of the indicator are considered (see Table 1 in Garaschuk et al. *(108)*).

Taken together, optical recordings already provide unique insights into brain activity and organization. Improvements in sensitivity or selectivity would make these methods even more powerful.

Acknowledgments

The authors are indebted to their collaborators Vicencio Davila, Amiram Grinvald, Kohtaro Kamino, Les Loew, Bill Ross, Brian Salzberg, Dejan Vucinic, Alan Waggoner, Matt Wachowiak, and Jian-young Wu for numerous discussions about optical methods. The experiments carried out in our laboratories were supported by NIH grants DC05259 and NS42739, Deutsche Forschungsgemeinschaft (SFB 391 and SFB 596) and the Bundesministerium für Bildung und Forschung (NGFN-2).

References

1. Cohen L.B., Salzberg B.M. (1978). Optical measurement of membrane potential. Rev Physiol Biochem Pharmacol, 83, 35–88.
2. Loew L.M., Cohen L.B., Salzberg B.M., Obaid A.L., Bezanilla F. (1985). Charge-shift probes of membrane potential. Characterization of aminostyrylpyridinium dyes on the squid giant axon. Biophys J, 47, 71–77.
3. Gupta R.K., Salzberg B.M., Grinvald A., Cohen L.B., Kamino K., Lesher S., Boyle M.B., Waggoner A.S., Wang C.H. (1981). Improvements in optical methods for measuring rapid changes in membrane potential. J. Membr. Biol., 58, 123–137.
4. Waggoner A.S., Grinvald A. (1977). Mechanisms of rapid optical changes of potential sensitive dyes. Annu NY Acad Sci, 303, 217–241.
5. Fromherz P., Dambacher K.H., Ephardt H., Lambacher A., Muller C.O., Neigl R., Schaden H., Schenk O., Vetter T. (1991). Fluorescent dyes as probes of voltage transients in neuron membranes: Progress report. Ber. Bunsenges. Phys. Chem., 95, 1333–1345.
6. Cohen L.B., Lesher, S. (1986). Optical monitoring of membrane potential: methods of multisite optical measurement. Soc Gen Physiol Ser, 40, 71–99.
7. Grinvald A., Frostig R.D., Lieke E., Hildesheim R. (1988) Optical imaging of neuronal activity. Physiological Reviews. 68: 1285–1366.
8. Nakashima M., Yamada S., Shiono S., Maeda M., Satoh F. (1992) 448-detector Optical Recording System: Development and application to *Aplysia* gill-withdrawal reflex. IEEE Trans Biomed Eng. 39: 26–36.
9. Momose-Sato Y., Sato K., Sakai T., Hirota A., Matsutani K., Kamino, K. (1995). Evaluation of optimal voltage-sensitive dyes for optical measurement of embryonic neural activity. J Memb. Biology, 144, 167–176.
10. Zecevic D. (1996). Multiple spike-initiation zones in single neurons revealed by voltage-sensitive dyes. Nature. 381: 322–325.
11. Palmer L.M., Stuart G.J. (2006) Site of action potential initiation in layer 5 pyramidal neurons. J Neurosci. 2006 Feb 8;26(6):1854–63.
12. Canepari M., Djurisic M., Zecevic D. (2007) Dendritic signals from rat hippocampal CA1 pyramidal neurons during coincident pre- and post-synaptic activity: a combined voltage- and calcium-imaging study. J Physiol. 580:463–484.
13. Neher E., Augustine G.J. (1992) Calcium gradients and buffers in bovine chromaffin cells. J Physiol. 450:273–301.
14. Helmchen F., Imoto K., Sakmann, B (1996) Ca^{2+} buffering and action potential-evoked $Ca^{2}+$ signaling in dendrites of pyramidal neurons. Biophys. J. 70:1069–1081.
15. Stuart G.J., Sakmann B. (1994). Active propagation of somatic action potentials into neocortical pyramidal cell dendrites. Nature 367, 69–72.
16. Spruston N., Schiller Y., Stuart G., Sakmann B. (1995). Activity-dependent action potential invasion and calcium influx into hippocampal CA1 dendrites. Science 268, 297–300.
17. Magee J.C., Johnston D. (1995). Synaptic activation of voltage-gated channels in the dendrites of hippocampal pyramidal neurons. Science, 268, 301–304.
18. Magee J.C., Christofi G., Miyakawa H., Christie B., Lasser-Ross N., Johnston D. (1995). Subthreshold synaptic activation of voltage-gated calcium channels mediate a localized calcium influx into dendrites

of hippocampal pyramidal neurons. J. Neurophysiol., 74, 335–324.
19. Stuart G.J., Hausser M. (2001) Dendritic coincidence detection of EPSPs and action potentials. Nat. Neurosci. 4:63–71.
20. Berger T., Larkum M.E., Luscher H.R. (2001) High I(h) channel density in the distal apical dendrite of layer V pyramidal cells increases bidirectional attenuation of EPSPs. J Neurophysiol 85: 855–868.
21. Antic S., Major G., Zecevic D. (1999) Fast optical recording of membrane potential changes from dendrites of pyramidal neurons. J. Neurophysiol., 82, 1615–1621.
22. Antic S., Wuskell J.P., Loew L., Zecevic D. (2000). Functional profile of the giant metacerebral neuron of *Helix aspersa*: Temporal and spatial dynamics of electrical activity in situ. J Physiol (Lond) *527*,55–69.
23. Antic S. (2003). Action potentials in basal and oblique dendrites of rat neocortical pyramidal neurons. J Physiol 550, 35–50.
24. Djurisic M., Antic S., Chen, W-r., Zecevic D. (2004) Voltage imaging from dendrites of mitral cells: EPSP attenuation and spike trigger zones. J. Neuroscience. 24, 6703–6714.
25. Antic S., Zecevic D. (1995). Optical signals from neurons with internally applied voltage- sensitive dyes. J Neuroscience, 15, 1392–1405.
26. Grinvald A., Hildesheim R., Farber I.C., Anglister L. (1982). Improved fluorescent probes for the measurement of rapid changes in membrane potential. Biophys J, 39, 301–308.
27. Ross W.N., Krauthamer V. (1984) Optical measurements of potential changes in axons and processes of neurons of a barnacle ganglion. J Neurosci 4: 659-672.
28. Grinvald A., Salzberg B. M., Lev-Ram V., Hildesheim R. (1987). Optical recording of synaptic potentials from processes of single neurons using intracellular potentiometric dyes. Biophys J. 51, 643–651.
29. Zecevic D., Antic S. (1998) Fast optical measurement of membrane potential changes at multiple sites on an individual nerve cell. Histochem J., 30:197–216.
30. Bischofberger J., Jonas P. (1997) Action potential propagation into the presynaptic dendrites of rat mitral cells. J Physiol (Lond) 504: 359–65.
31. Chen W.R., Midtgaard J., Shepherd G.M. (1997). Forward and backward propagation of dendritic impulses and their synaptic control in mitral cells. Science 278, 463–467.
32. Christie J.M., Westbrook G.L. (2003) Regulation of backpropagating action potentials in mitral cell lateral dendrites by A-type potassium currents. J Neurophysiol 89: 2466–2472.
33. Davila H.V., Salzberg B.M., Cohen L.B., Waggoner A.S. (1973). A large change in axon fluorescence that provides a promising method for measuring membrane potential. Nature, New Biol., 241, 159–160.
34. Tsien R.W., Tsien R.Y. (1990). "Calcium channels, stores, and oscillations." Annu. Rev. Cell Biol. 6: 715–760.
35. Berridge M.J., Lipp P., Bootman M.D. (2000). "The versatility and universality of calcium signaling." Nat. Rev. Mol. Cell. Biol. 1: 11–21.
36. Verkhratsky A. (2005). "Physiology and pathophysiology of the calcium store in the endoplasmic reticulum of neurons." Physiol. Rev. 85: 201–279.
37. Tsien R.Y. (1981). "A non-disruptive technique for loading calcium buffers and indicators into cells." Nature 290: 527–528.
38. Stosiek C., Garaschuk O., Holthoff K., Konnerth A. (2003) In vivo two-photon calcium imaging of neuronal networks. Proc. Natl. Acad. Sci. U S A. 100:7319–7324.
39. Brustein E., Marandi N., Kovalchuk Y., Drapeau P., Konnerth A. (2003). "'In vivo' monitoring of neuronal network activity in zebrafish by two-photon Ca^{2+} imaging." Pflugers Arch. 446: 766–773.
40. Nimmerjahn A., Kirchhoff F., Kerr J.N.D., Helmchen F. (2004). "Sulforhodamine 101 as a specific marker of astroglia in the neocortex in vivo." Nature Methods 1: 31–37.
41. Kerr J.N., Greenberg D., Helmchen F. (2005). "Imaging input and output of neocortical networks in vivo." Proc. Natl. Acad. Sci. U S A 102: 14063–14068.
42. Li J., Mack J.A., Souren M., Yaksi E., Higashijima S., Mione M., Fetcho J.R., Friedrich R.W. (2005). "Early development of functional spatial maps in the zebrafish olfactory bulb." J. Neurosci. 25: 5784–5795.
43. Niell C.M., S.J. Smith (2005). "Functional imaging reveals rapid development of visual response properties in the zebrafish tectum." Neuron 45: 941–951.
44. Ohki K., Chung S., Ch'ng Y.H., Kara P., Reid R.C. (2005). "Functional imaging with cellular resolution reveals precise microarchitecture in visual cortex." Nature 433: 597–603.
45. Sullivan M.R., Nimmerjahn A., Sarkisov D.V., Helmchen F., Wang S.S. (2005). "In vivo calcium imaging of circuit activity in cerebellar cortex." J. Neurophysiol. 94: 1636–1644.

46. Garaschuk O., Milos R.I., Grienberger C., Marandi N., Adelsberger H., Konnerth A. (2006). "Optical monitoring of brain function in vivo: From neurons to networks." Pflugers Arch. 453: 385–396.
47. Xu F., Kida I., Hyder F., Shulman R. (2000) Assessment and discrimination of odor stimuli in rat olfactory bulb by dynamic functional MRI. Proc Natl Acad Sci USA 97:10601–10606.
48. Woo C.C., Hingco E.E., Johnson B.A., Leon M. (2007) Broad activation of the glomerular layer enhances subsequent olfactory responses. Chemical Senses, 32: 51–55.
49. Rubin B., Katz L. (1999) Optical imaging of odorant representations in the mammalian olfactory bulb. Neuron 23:499–511.
50. O'Donovan M.J., Sholomenko S.Ho.G., Yee W. (1993). Real-time imaging of neurons retrogradely and anterogradely labeled with calcium-sensitive dyes. J. Neuroscience Methods, 46, 91–106.
51. Tsau Y., Wenner P., O'Donovan M.J., Cohen L.B., Loew L.M., Wuskell, J.P.. (1996). Dye screening and signal-to-noise ratio for retrogradely transported voltage-sensitive dyes. J. Neuroscience Methods, 70, 121–129.
52. Kreitzer A.C., Gee K.R., Archer E.A., Regehr W.G. (2000) Monitoring presynaptic calcium dynamics in projection fibers by in vivo loading of a novel calcium indicator. Neuron. 27, 25–32.
53. Friedrich R.W., Korsching S.I., (1997) Combinatorial, and chemotropic odorant coding in the zebrafish olfactory bulb visualized by optical imaging. Neuron, 18, 737–752.
54. Wachowiak M., Cohen L.B., (2001) . Representation of odorants by receptor neuron input to the mouse olfactory bulb. Neuron, Neuron, 32: 725–737.
55. Yaksi E., Friedrich R.W. (2006) Reconstruction of firing rate changes across neuronal populations by temporally deconvolved Ca^{2+} imaging. Nat. Methods. 5:377–383.
56. Vucinic D., Cohen L.B., and Kosmidis E.K. (2004), Presynaptic center-surround inhibition shapes sensory input to the mouse olfactory bulb. J. Neurophysiology, 2006 95:1881–1887.
57. Lam Y.-W., Cohen L.B., Wachowiak M., Zochowski M.R., (2000), Odors elicit three different oscillations in the turtle olfactory bulb. J. Neuroscience, 20:749–762.
58. Wachowiak M., Cohen L.B., (1999), Presynaptic inhibition of primary olfactory afferents mediated by different mechanisms in the lobster and turtle. J. Neuroscience, 19, 8808–8817.
59. Ross W.N., B.M. Salzberg L.B. Cohen A. Grinvald H.V. Davila A.S. Waggoner, Wang C.H. (1977). Changes in absorption, fluorescence, dichroism, and birefringence in stained giant axons : Optical measurement of membrane potential. J Memb. Biol, 33, 141–183.
60. Boyle M.B., Cohen L.B. (1980). Birefringence signals that monitor membrane potential in cell bodies of molluscan neurons. Fed Proc, 39, 2130.
61. Orbach H.S., Cohen L.B. (1983). Optical monitoring of activity from many areas of the in vitro and in vivo salamander olfactory bulb: A new method for studying functional organization in the vertebrate central nervous system. J Neuroscience, 3, 2251–2262.
62. Orbach H.S., Cohen L.B., Grinvald A. (1985). Optical mapping of electrical activity in rat somatosensory and visual cortex. J Neuroscience, 5, 1886–1895.
63. Grynkiewicz G., Poenie M., Tsien R.Y. (1985) A new generation of Ca^{2+} indicators with greatly improved fluorescence properties. J Biol Chem. 260:3440–3450.
64. Gross E., Bedlack R.S., Loew L.M. (1994). Dual-wavelength ratiometric fluorescence measurements of the membrane dipole potential. Biophysical J. 67, 208–216.
65. Braddick H.J.J. (1960). Photoelectric photometry. Rep Prog Physics, 23, 154–175.
66. Malmstadt H.V., Enke C.G., Crouch S.R., Harlick G.. (1974). Electronic Measurements for scientists, Benjamin, Menlo Park, CA.
67. Helmchen F., Denk W. (2005). "Deep tissue two-photon microscopy." Nat. Methods 2: 932–940.
68. Salzberg B.M., Grinvald A., Cohen L.B., Davila H.V., Ross W.N. (1977). Optical recording of neuronal activity in an invertebrate central nervous system: Simultaneous monitoring of several neurons. J Neurophysiol, 40, 1281–1291.
69. London J.A., Zecevic D., Cohen, L.B.. (1987). Simultaneous optical recording of activity from many neurons during feeding in *Navanax*. J Neurosci, 7, 649–661.
70. Svoboda K., Denk W., Kleinfeld D., Tank D.W. (1997). "In vivo dendritic calcium dynamics in neocortical pyramidal neurons." Nature 385: 161–165.
71. Denk W., Svoboda K. (1997). "Photon upmanship: Why multiphoton imaging is more than a gimmick." Neuron 18: 351–357.
72. Svoboda K., Yasuda R. (2006). "Principles of two-photon excitation microscopy and its

applications to neuroscience." Neuron 50: 823–839.
73. Inoue S. (1986) Video Microscopy. Plenum Press, New York. p 128.
74. Kleinfeld D., Delaney K.R.. (1996). Distributed representation of vibrissa movement in the upper layers of somatosensory cortex revealed with voltage-sensitive dyes. J Comparative Neurology, 375, 89–108.
75. Cohen L.B., Keynes R.D. (1971). Changes in light scattering associated with the action potential in crab nerves. J. Physiol (Lond), 212, 259–275.
76. Petran M., Hadravsky M. (1966). Czechoslovakian patent 7720.
77. Denk W, Strickler J.H., Webb W.W. (1990). "Two-photon laser scanning fluorescence microscopy." Science 248: 73–76.
78. Yuste R., W. Denk. (1995). Dendritic spines as basic functional units of neuronal integration. Nature 375, 682–684.
79. Loew L.M. (1993). Confocal microscopy of potentiometric fluorescent dyes. Methods Cell Biol 38, 195–209.
80. Shaw R. (1979). Photographic detectors. Appl Optics Optical Eng, 7, 121–154.
81. Hamer F.M. (1964). The Cyanine Dyes and Related Compounds, Wiley, New York.
82. Loew L.M., Cohen L.B., Dix J., Fluhler E.N., Montana V., Salama G., Wu J.Y. (1992). A napthyl analog of the aminostyryl pyridinium class of potentiometric membrane dyes shows consistent sensitivity in a variety of tissue, cell, and model membrane preparations. J Memb. Biology, 130, 1–10.
83. Rohr S., Salzberg B.M. (1994). Multiple site optical recording of transmembrane voltage in patterned growth heart cell cultures: assessing electrical behavior, with microsecond resolution, on a cellular and subcellular scale. Biophys J. 67, 1301–1315.
84. Gonzalez J.E., Tsien R.Y. (1995). Voltage sensing by fluorescence energy transfer in single cells. Biophysical J, 69, 1272–1280.
85. Cacciatore T.W., Brodfuehrer P.D., Gonzalez J.E., Jiang T., Adams S.R., Tsien R.Y., Kristan W.B. Jr., Kleinfeld D. (1999) Identification of neural circuits by imaging coherent electrical activity with FRET-based dyes. Neuron. 23: 449–459.
86. Briggman K.L., Kristan W.B. (2006) Imaging dedicated and multifunctional neural circuits generating distinct behaviors. J Neurosci. 26:10925–10933.
87. Bouevitch O., Lewis A., Pinevsky I., Wuskell J., Loew L. (1993). Probing membrane potential with non-linear optics. Biophysical J, 65, 672–679.
88. Millard A.C., Jin L., Wuskell J.P., Boudreau D.M., Lewis A., Loew L.M. (2005) Wavelength- and time-dependence of potentiometric non-linear optical signals from styryl dyes. J Membr Biol. 208:103–111.
89. Dombeck D.A., Sacconi L., Blanchard-Desce M., Webb W. W. (2005) Optical recording of fast neuronal membrane potential transients in acute mammalian brain slices by second-harmonic generation microscopy. J Neurophysiol. 94:3628–3636.
90. Hickie C., Wenner P., O'Donovan M., Tsau Y., Fang J., Cohen L.B. (1996). Optical monitoring of activity from individual and identified populations of neurons retrogradely labeled with voltage-sensitive dyes. Abs Soc Neuroscience, 22, 321.
91. Nirenberg S., Cepko C. (1993). Targeted ablation of diverse cell classes in the nervous system in vivo. J Neuroscience, 13, 3238–3251.
92. Siegel M.S., Isacoff E.Y., (1997) A genetically encoded optical probe of membrane voltage. Neuron 19:735–41.
93. Ataka K., Pieribone V.A. (2002) A genetically-targetable fluorescent probe of channel gating with rapid kinetics. Biophysical J., 82, 509–516.
94. Baker B.J., Lee H., Pieribone V.A., Cohen L.B., Isacoff E.Y., Knopfel T., Kosmidis E.K. (2007) Fluorescent protein voltage sensors exhibit low plasma membrane expression in mammalian cells. J. Neuroscience Methods, 161: 32–38.
95. Dimitrov D., He Y., Mutoh H., Baker B.J., Cohen L. Akemann W., and Knopfel T. (2007) Engineering and characterization of an enhanced fluorescent protein voltage sensor. PLOS One, 2(5); e440.
96. Murata Y, Iwasaki H, Sasaki M, Inaba K, Okamura Y (2005) Phosphoinositide phosphatase activity coupled to an intrinsic voltage sensor. Nature 435: 1239–1243.
97. Baird G.S., Zacharias D.A., Tsien R.Y. (1999). "Circular permutation and receptor insertion within green fluorescent proteins." Proc. Natl. Acad. Sci. U S A 96: 11241–11246.
98. Nagai T., Sawano A., Park E.S., Miyawaki A. (2001). "Circularly permuted green fluorescent proteins engineered to sense Ca^{2+}." Proc. Natl. Acad. Sci. U S A 98: 3197–3202.
99. Nakai J., Ohkura M., Imoto K. (2001). "A high signal-to-noise Ca^{2+} probe composed of a single green fluorescent protein." Nat. Biotechnol. 19: 137–141.
100. Zhang J., Campbell R.E., Ting A.Y., Tsien R.Y. (2002). "Creating new fluorescent

probes for cell biology." Nat Rev Mol Cell Biol 3(12): 906–918.
101. Ohkura M., Matsuzaki M., Kasai H., Imoto K., Nakai J. (2005). "Genetically encoded bright Ca^{2+} probe applicable for dynamic Ca^{2+} imaging of dendritic spines." Anal. Chem. 77: 5861–5869.
102. Reiff D.F., Ihring A., Guerrero G., Isacoff E.Y., Joesch M., Nakai J., Borst A. (2005). "In vivo performance of genetically encoded indicators of neural activity in flies." J. Neurosci. 25: 4766–4778.
103. Miyawaki A., Llopis J., Heim R., McCaffery J.M., Adams J.A., Ikura M., Tsien R.Y. (1997). "Fluorescent indicators for Ca^{2+} based on green fluorescent proteins and calmodulin." Nature 388: 882–887.
104. Miyawaki A. (2005). "Innovations in the imaging of brain functions using fluorescent proteins." Neuron 48: 189–199.
105. Hasan M.T., Friedrich R.W., Euler T., Larkum M.E., Giese G., Both M., Duebel J., Waters J., Bujard H., Griesbeck O., Tsien R.Y., Nagai T., Miyawaki A., Denk W. (2004). "Functional fluorescent Ca^{2+} indicator proteins in transgenic mice under TET control." PLoS Biol. 2: 763–775.
106. Nagai T., Yamada S., Tominaga T., Ichikawa M., Miyawaki A. (2004). "Expanded dynamic range of fluorescent indicators for $Ca^{2+}$by circularly permuted yellow fluorescent proteins." Proc. Natl. Acad. Sci. U S A 101: 10554–10559.
107. Diez-Garcia J., Matsushita S., Mutoh H., Nakai J., Ohkura M., Yokoyama J., Dimitrov D., Knopfel T. (2005). "Activation of cerebellar parallel fibers monitored in transgenic mice expressing a fluorescent Ca^{2+} indicator protein." Eur. J. Neurosci. 22: 627–635.
108. Garaschuk O., Griesbeck O., Konnerth A. (2007). "Troponin C-based biosensors: A new family of genetically encoded indicators for in vivo calcium imaging in the nervous system." Cell Calcium. in press.
109. Heim N. and O. Griesbeck (2004). "Genetically encoded indicators of cellular calcium dynamics based on troponin C and green fluorescent protein." J. Biol. Chem. 279: 14280–14286.
110. Mank M., Reiff D.F., Heim N., Friedrich M.W., Borst A., Griesbeck O. (2006). "A FRET-based calcium biosensor with fast signal kinetics and high fluorescence change." Biophys. J. 90: 1790–1796.
111. Heim N., Garaschuk O., Friedrich M.W., Mank M., Milos R.I., Kovalchuk Y., Konnerth A., Griesbeck O. (2007). "Improved calcium imaging in transgenic mice expressing a troponin-C based biosensor." Nature Methods 4: 127–129.
112. Garaschuk O., Milos R.I., Konnerth A. (2006). "Targeted bulk-loading of fluorescent indicators for two-photon brain imaging in vivo." Nat. Prot. 1: 380–386.